

Supporting Information

Customizable Crystalline-Amorphous Rectifying Heterostructure Cathodes for Durable and Super-Fast Zinc Storage

Ming Yang,^{a1} Mingyan Chuai,^{bc1} Mengnan Lai,^a Jianhui Zhu,^a Yanyi Wang,^{*a} Qicheng Hu,^a Minfeng Chen,^d Jizhang Chen,^d Kang Fang,^e Guoliang Chai,^{bc} Hongwei Mi,^a Lingna Sun,^a Chuanxin He,^a Dingtao Ma,^{*a} and Peixin Zhang^{*a}

^a College of Chemistry and Environmental Engineering, Shenzhen University, Shenzhen 518060, P. R. China.

E-mail: wyy1984@szu.edu.cn; mdt2500@szu.edu.cn; pxzhang@szu.edu.cn

^b State Key Laboratory of Structural Chemistry, Fujian Institute of Research on the Structure of Matter, Chinese Academy of Sciences.

^c Mindu Innovation Laboratory, Fujian Science & Technology Innovation Laboratory for Optoelectronic Information of China, Fuzhou 350108, Fujian, P. R. China.

^d College of Materials Science and Engineering, Nanjing Forestry University, Nanjing 210037, P. R. China

^e Guangdong Provincial Key Laboratory of Semiconductor Optoelectronic Materials and Intelligent Photonic Systems, School of Materials Science and Engineering, Harbin

Institute of Technology, Shenzhen, Shenzhen 518055, P. R. China

Experimental Section

Materials Synthesis

Preparation of the VSSe, VS_{1.5}Se_{0.5}, VS_{0.5}Se_{1.5} and MnS_{0.5}Se_{0.5} materials

The VSSe material is prepared by mixing vanadium powder or manganese powder, sulfur powder and selenium powder, then vacuum sealed in a quartz tube, and then calcined at 900°C for 2 days.

Material characterizations

The crystal structure was determined using the X-ray diffractometer with Cu K α radiation (PANalytical). The morphology and microstructure of the VSSe nanoparticles were characterized by employing the Scanning Electron Microscope (Thermo Scientific Apreo S) and multipurpose electron microscope (JEM-F200). The nitrogen adsorption-desorption isotherms were measured by BELSORP-max Surface Area and Pore Porosimeter. The in-situ Raman measurements on the cathode side were carried out on a confocal Raman spectroscope (Renishaw inVia) coupled with a LAND CT3002A battery testing instrument. The wettability of the water and sample was measured by a dynamic contact angle test (JC2000D2, POWEREACH, China). Fourier transform infrared spectra (FTIR) were recorded using an IR Affinity⁻¹ spectrometer. The valence state of elements was measured by an X-ray photoelectron spectroscope (Thermo Fisher, K-Alpha+).

Electrochemical performance tests

Electrochemical measurements were carried out by assembling the CR2032 coin cells. active materials, acetylene black, and polyvinylidene fluoride (PVDF) were added into NMP solvent at a weight ratio 7:2:1 and continued stirring to obtain the slurry mixture. Subsequently, the as-prepared slurry was cast onto the Ti foil collector and dried at 80 °C under vacuum for 12 h to obtain the cathode. Zinc foil, glass fiber, and 3 M Zn(CF₃SO₃)₂ aqueous solution were selected as the anode, separator, and electrolyte, respectively. Note that all the electrochemical measurements of the electrodes were conducted at the average mass loading of ~1-2 mg cm⁻². Cyclic voltammetry (CV)

measurement was tested on a Solartron 1470E electrochemical station at a scan rate from 0.2 to 100 mV s⁻¹. A galvanostatic charge/discharge test was performed from 0.1 to 1.5, 1.6, 1.8 and 2.0 V on a LAND CT3002A. In-situ EIS measurement was tested on the Solartron electrochemical station. The data was collected at different cycles with a current density of 1 A g⁻¹. The impedance test frequency is 0.01-10⁶ Hz.

DFT calculation

All the calculations are implemented using the VASP code. The GGA-PBE functional is selected for the exchange and correlation potential. Weak van der Waals interaction is considered by the DFT-D3 functional. The cut-off energy for the plane wave is 350 eV. The 5 x 5 x 1 and 5 x 4 x 1 k-mesh in the Brillouin zone are chosen for integration. The total energies of the systems converge to 10⁻⁵ eV in the iteration solution of the Kohn-Sham equation. The force on each atom was reduced to 0.05 eV/Å after geometry optimization.

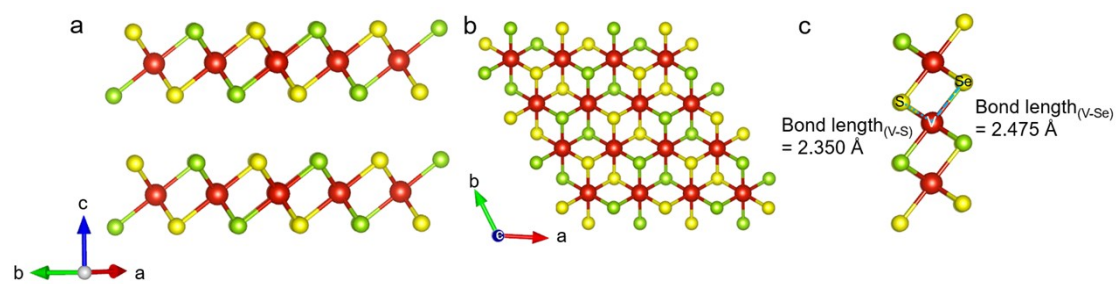


Figure S1. The crystal structure of VSSe. a) In-plane, b) Cross-plane, and c) The bond-length V-S and V-Se.



Figure S2. The batch preparation of VSSe via PVT method. a) The mixture of V, S and Se powder sealed in vacuum tube, b-d) The obtain product after annealing.

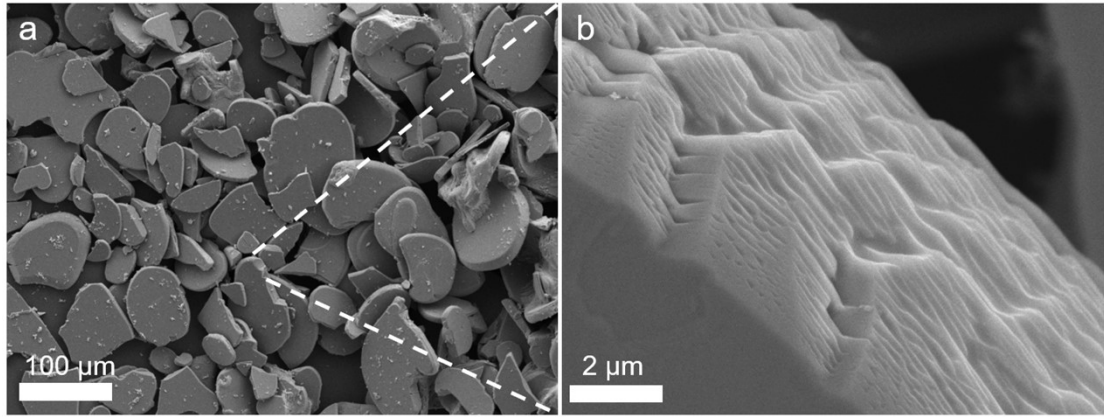


Figure S3. The SEM images of VSSe material a) Low magnification, b) High magnification.

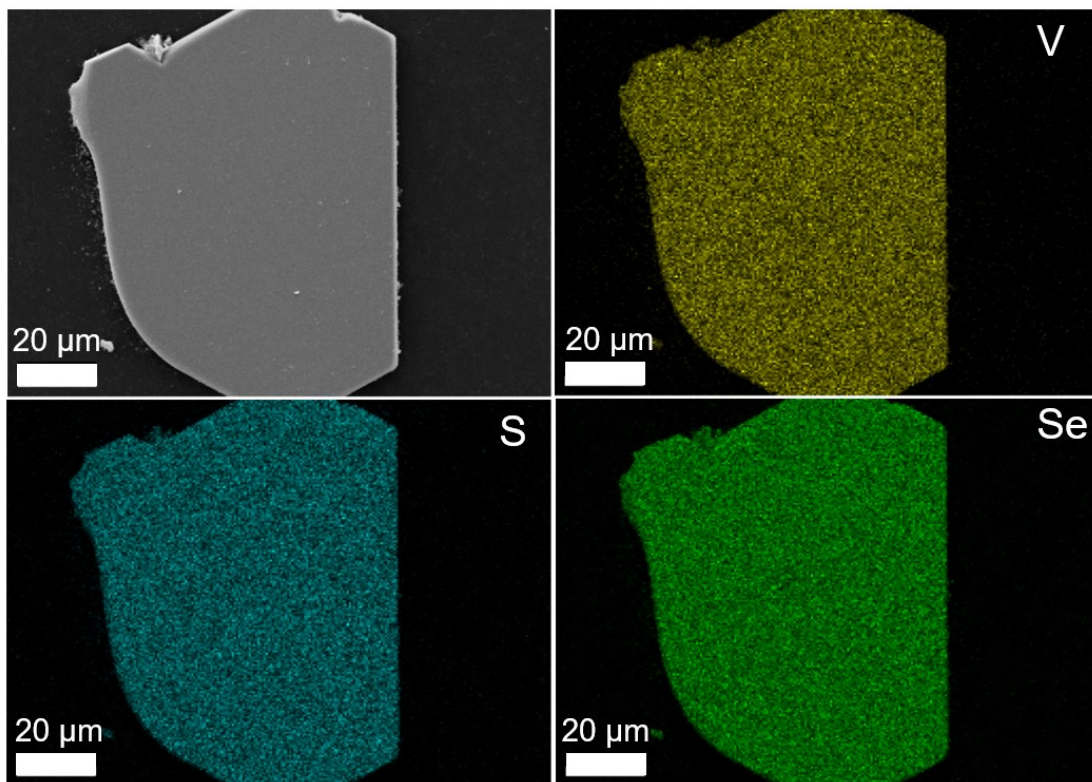


Figure S4. The EDS mappings of VSSe a) SEM image, b) V element, c) S element, d) Se element.

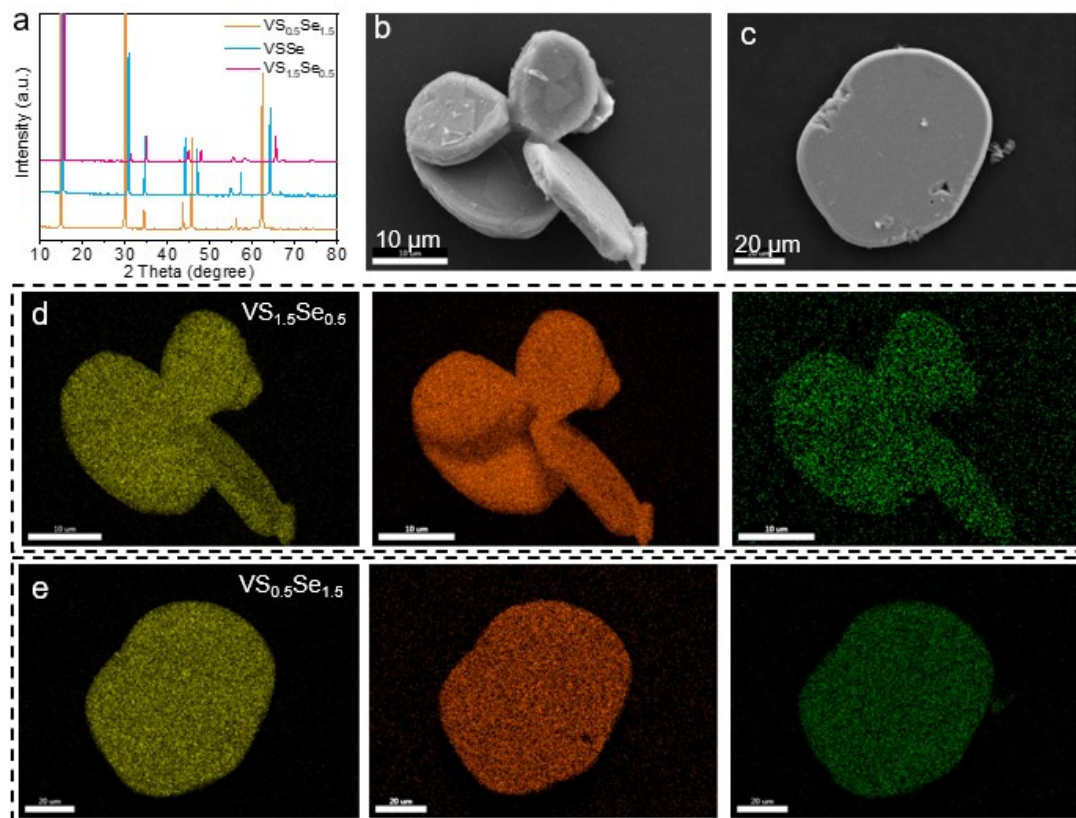


Figure S5. a) The XRD patterns of VS_{1.5}Se_{0.5}, VSSe and VS_{0.5}Se_{1.5}, b, d) The SEM image and EDS mappings of VS_{1.5}Se_{0.5}. c, e) The SEM image and EDS mappings of VS_{0.5}Se_{1.5}.

The VS_{1.5}Se_{0.5} and VS_{0.5}Se_{1.5} are synthesized via adjusting the molar ratio of V, S and Se, as shown in Figure S5, the diffraction peaks of VS_xSe_{2-x} ($x=0.5, 1$, and 1.5) all show sharp peaks, and as the content of S increases, the XRD diffraction peaks of VS_xSe_{2-x} gradually shift to the right. This is mainly due to the smaller atomic radius of S compared to Se. Subsequently, the SEM morphologies of VS_{1.5}Se_{0.5} and VS_{0.5}Se_{1.5} are similar to those of VSSe. Moreover, EDS mappings show that the distribution of V, S and Se elements in these two compounds is uniform, further suggesting that the synthesized samples are of pure phase.

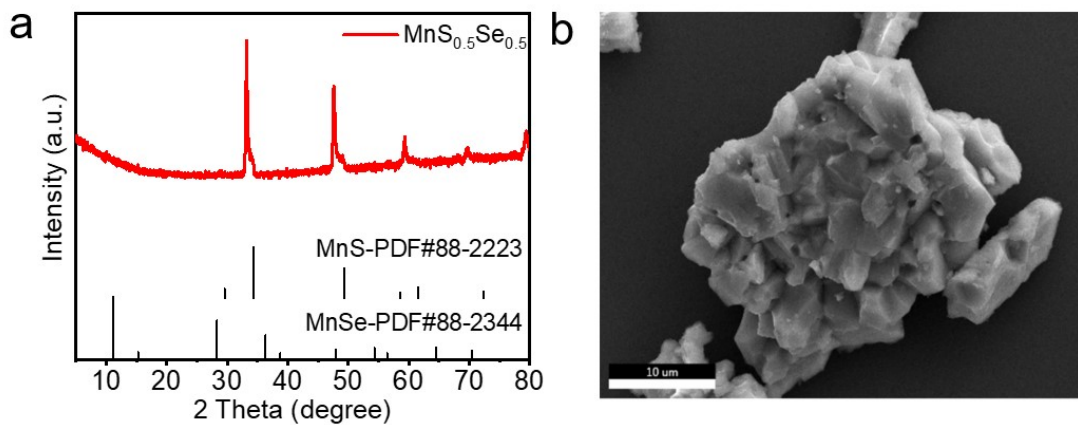


Figure S6. a) The XRD pattern and b) SEM image of $\text{MnS}_{0.5}\text{Se}_{0.5}$.

The synthesis of $\text{MnS}_{0.5}\text{Se}_{0.5}$ material is the same as that of VSSe . The diffraction pattern of MnSSe material is located between the standard cards of MnS and MnSe , and no other peaks are observed. This suggests that $\text{MnS}_{0.5}\text{Se}_{0.5}$ is a pure phase. The SEM image shows that MnSSe is in the form of aggregated particles.

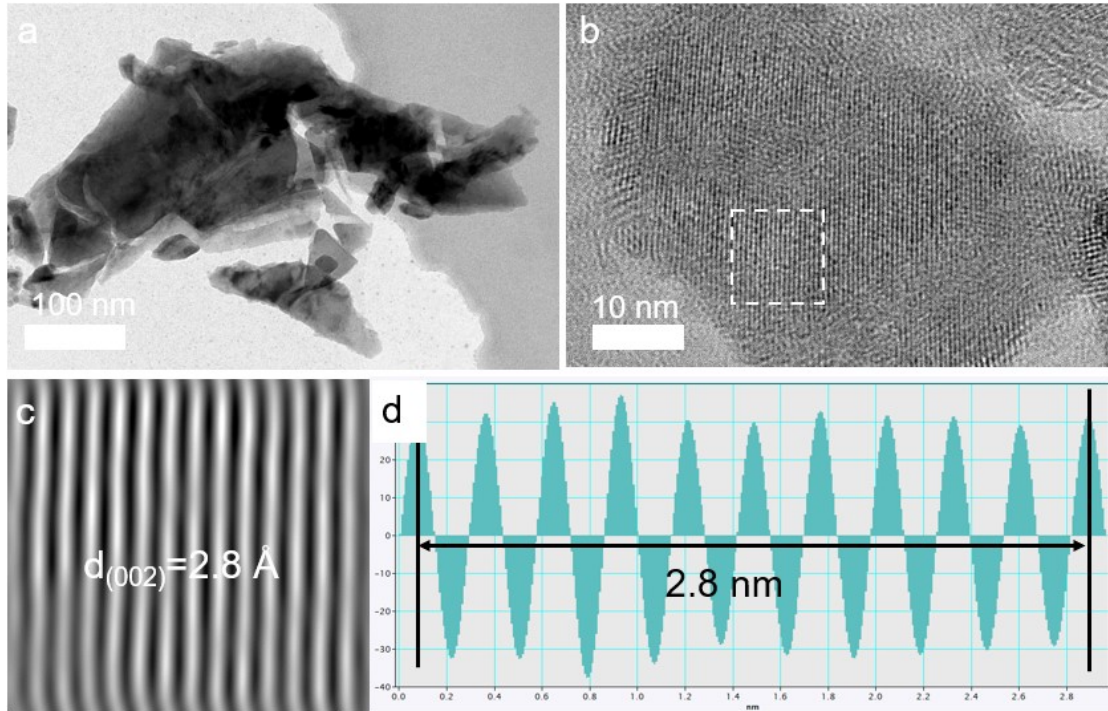


Figure S7. a) The TEM image, b) HRTEM image, c-d) Enlarged view of the selected part of the HRTEM image of VSSe material.

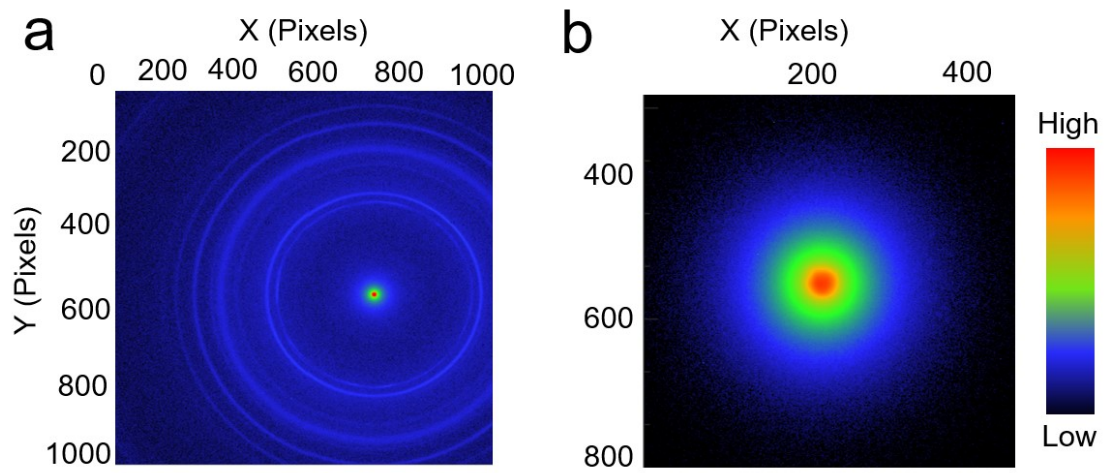


Figure S8. a) The WAXS image, b) the SAXS image of VSSe material.

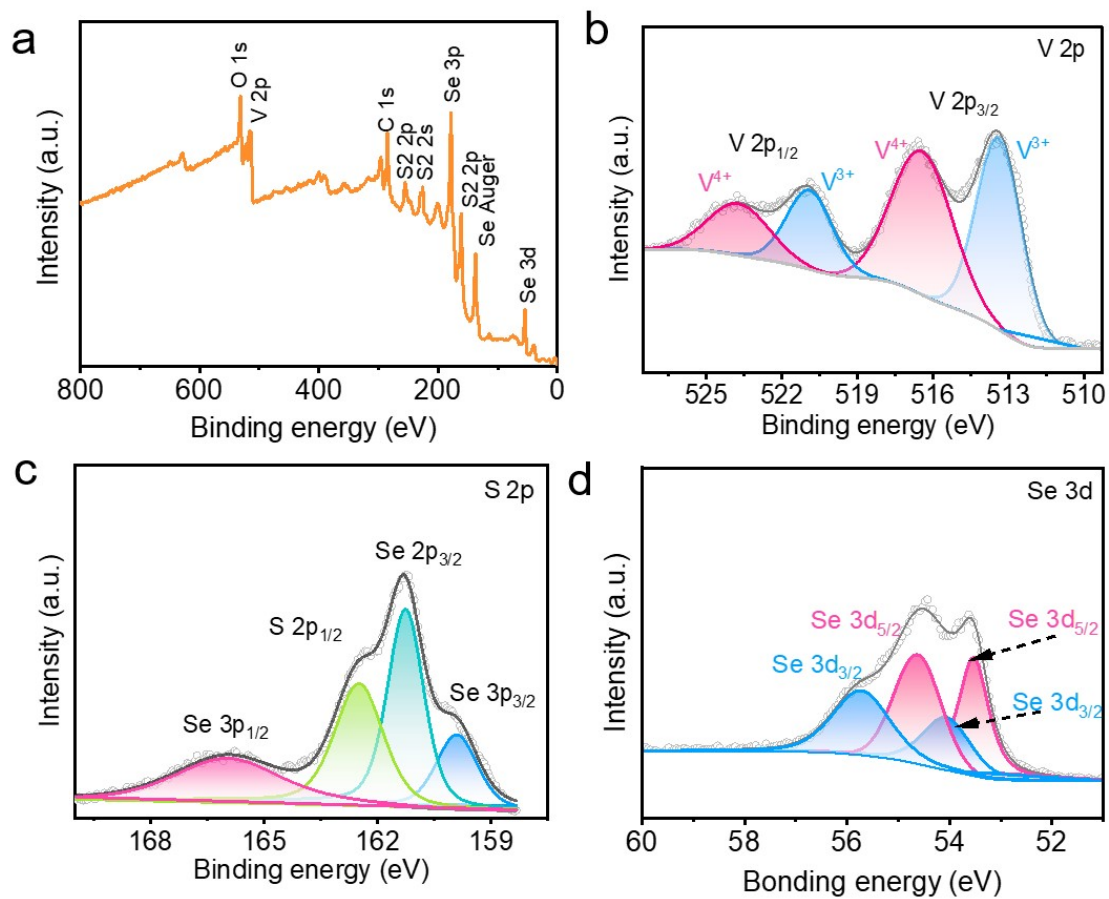


Figure S9. a) The survey XPS spectra, XPS high-resolution spectra b) V 2p, c) S 2p and d) Se 3d of VSSe material.

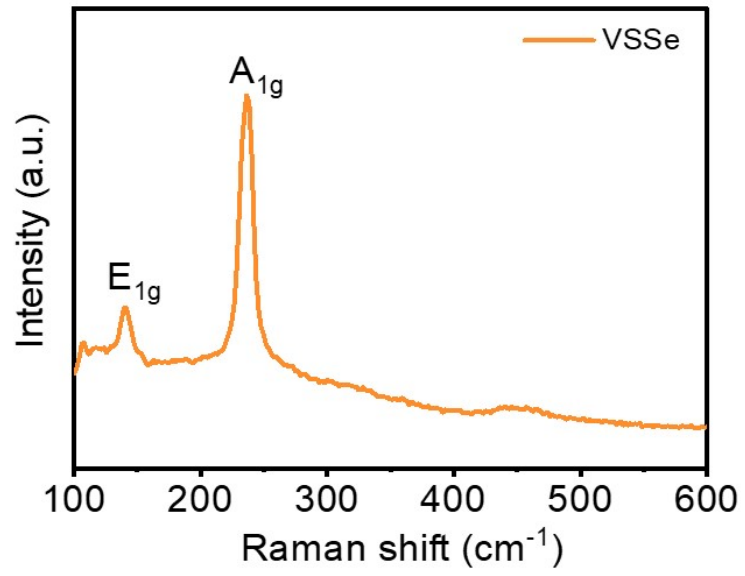


Figure S10. Raman spectra of VSSe material.

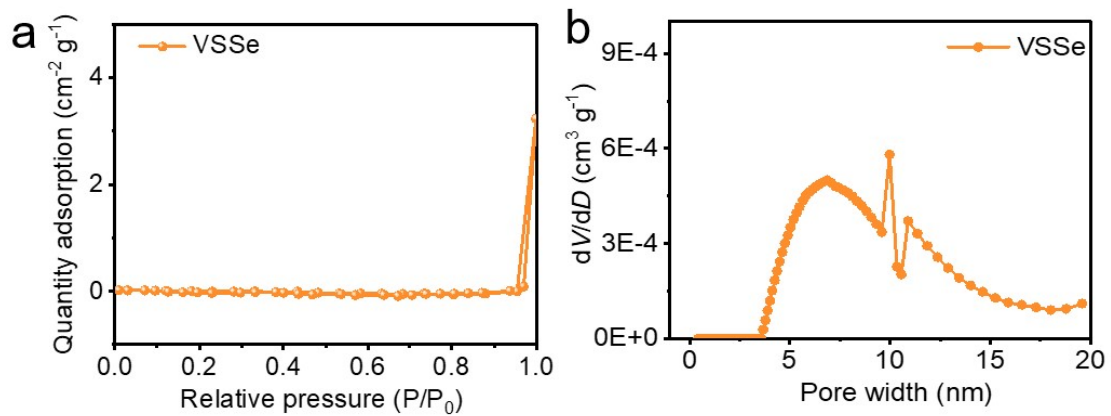


Figure S11. a) N₂ adsorption-desorption isotherms, b) Pore size distribution curves of VSSe material.

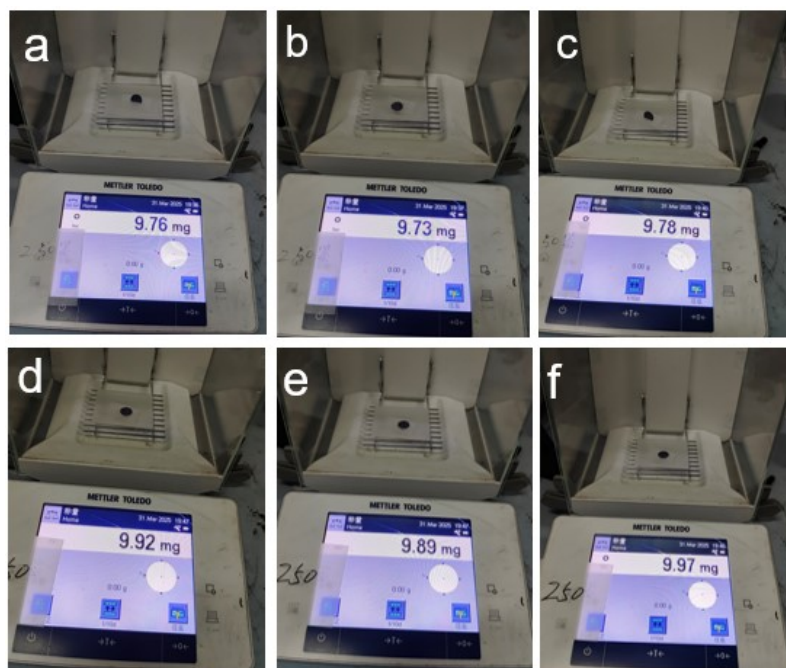


Figure S12. The mass of VSSe electrode (a-c) after rolling, (d-f) before rolling.

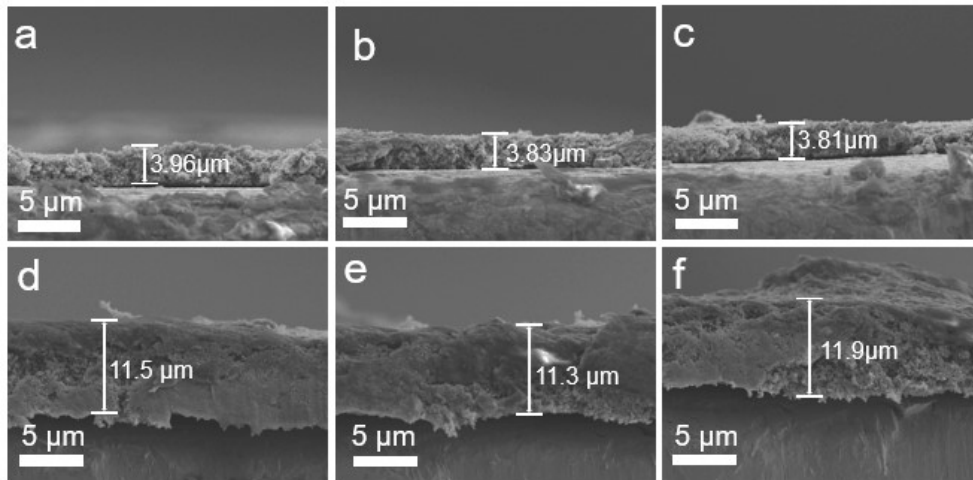


Figure S13. (a-c) The SEM images of VSSe electrode mass after rolling, (d-f) The SEM images of VSSe electrode mass before rolling.

The electrode density and tap density using the following parameters:

Electrode Area: 1.13 cm^2 (A round shape with a diameter of 12 mm)

The mass of titanium foil is 8.46 mg

Electrode Mass: 1.46 mg, 1.43 mg, and 1.51 mg (average: 1.47 mg).

After rolling Electrode Mass: 1.30 mg, 1.27 mg, and 1.32 mg (average: 1.30 mg).

Electrode Thickness: 11.5 μm , 11.3 μm , 11.9 μm average: 11.57 μm).

After rolling Electrode Thickness: 3.96 μm , 3.83 μm , 3.81 μm (average: 3.87 μm).

Electrode Density Calculation:

$$\begin{aligned} \text{Electrode Density} &= \frac{\text{Mass}}{\text{Area} \times \text{Thickness}} \\ &= \frac{1.47 \times 0.001 \text{ g}}{1.13 \text{ cm}^2 \times 11.57 \times 0.0001 \text{ cm}} = 1.12 \text{ g cm}^{-3} \end{aligned}$$

Tap Density Calculation:

$$\text{Tap Density} = \frac{\text{Mass}}{\text{Area} \times \text{Thickness}} = \frac{1.30 \times 0.001 \text{ g}}{1.13 \text{ cm}^2 \times 3.87 \times 0.0001 \text{ cm}} = 2.97 \text{ g cm}^{-3}$$

The calculated electrode density and tap density of the VSSe- V_2O_5 electrode is 1.12 g cm^{-3} and 2.97 g cm^{-3} , respectively.

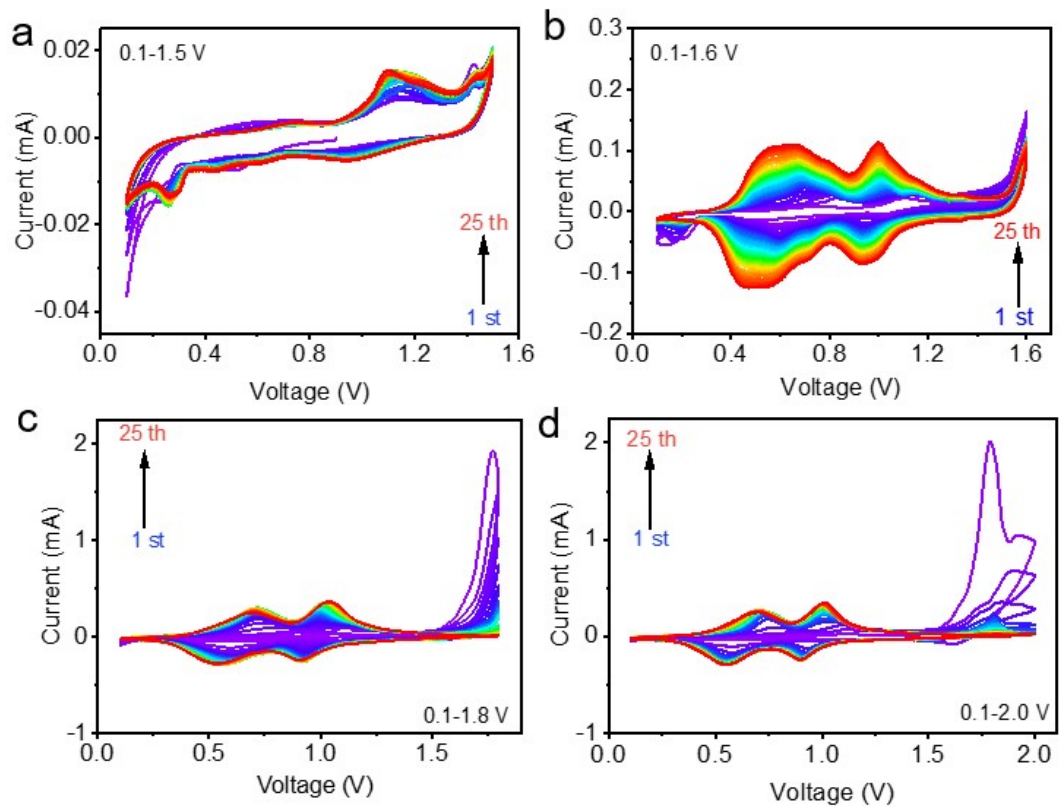


Figure S14. The first 25 cycles of CV curves of the VSSe electrode recorded in the voltage range of (a) 0.1-1.5 V, (b) 0.1-1.6 V, (c) 0.1-1.8 V, (d) 0.1-2.0 V, at the scan rate of 0.1 mV s^{-1} .

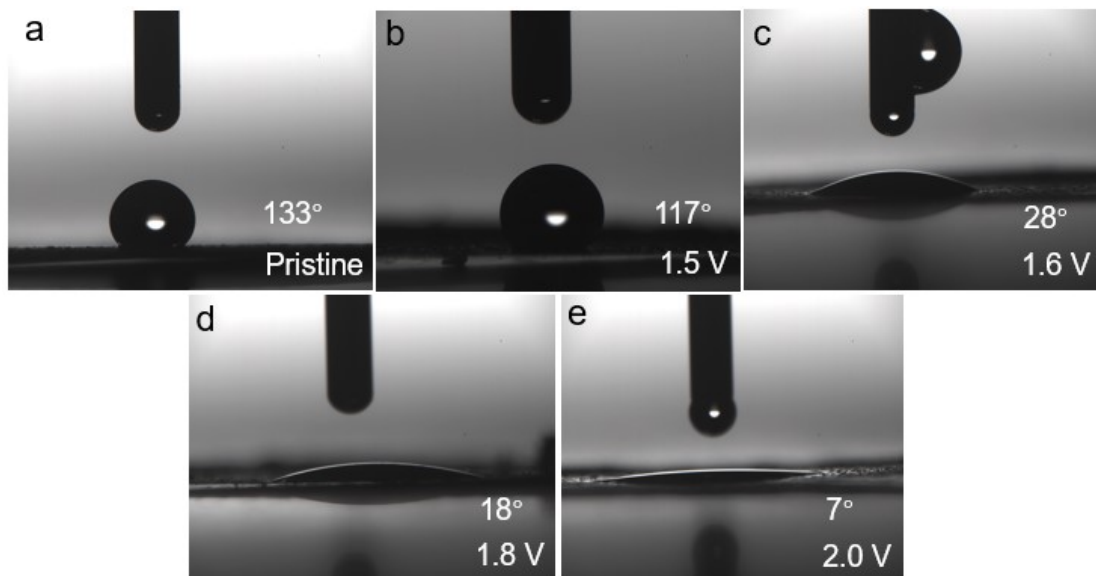


Figure S15. The contact angle of VSSe electrodes a) at pristine and the charged voltage of b) 1.5 V, c) 1.6 V, d) 1.8 V, and e) 2.0 V.

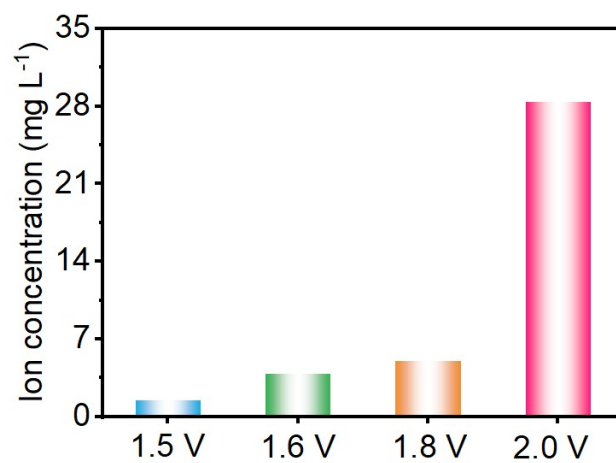


Figure S16. The V dissolution results of VSSe electrodes after cycling 5th with cut-off voltages of 1.5 V, 1.6 V, 1.8 V and 2.0 V.

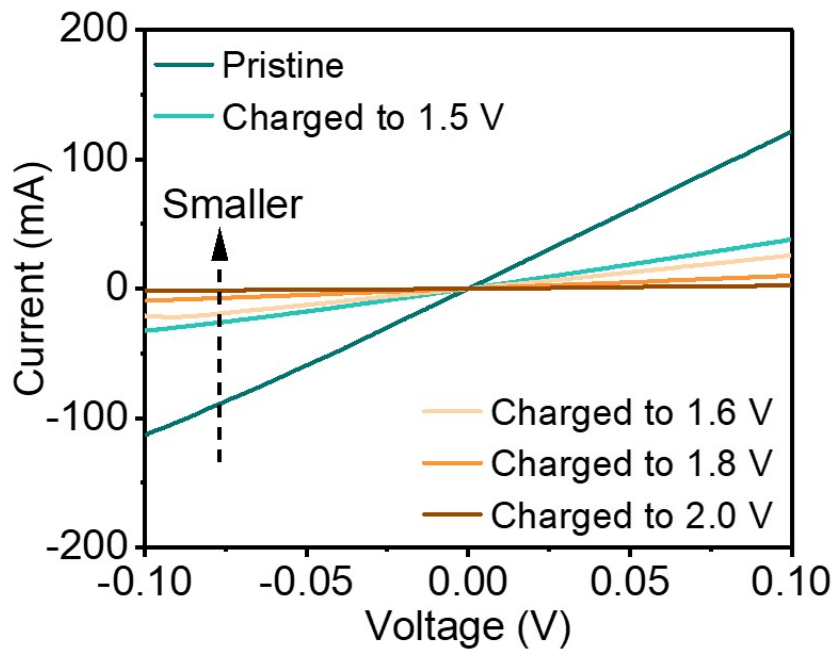


Figure S17. I-V curves of VSSe material at the voltage of 1.5 V, 1.6 V, 1.8 V and 2.0 V.

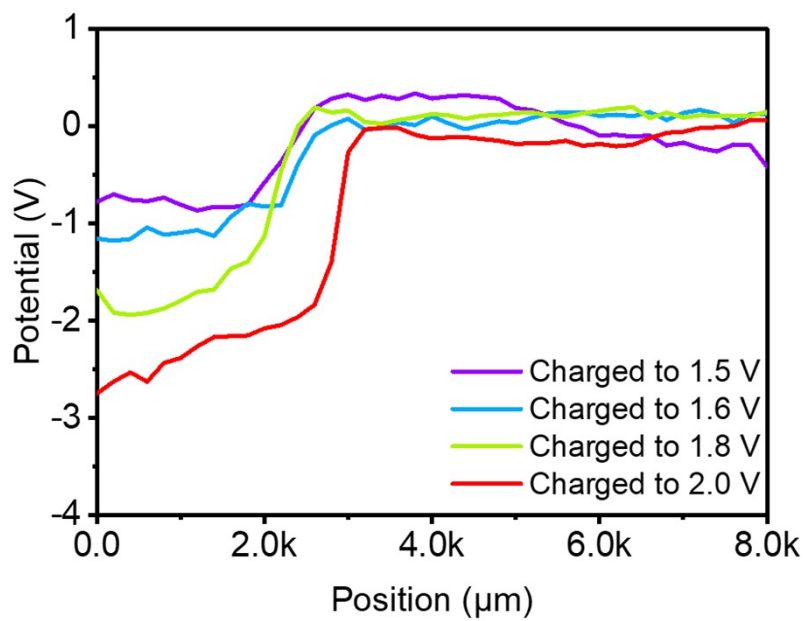


Figure S18. The SKP linear scanning of VSSe electrodes with various cut-off voltages.

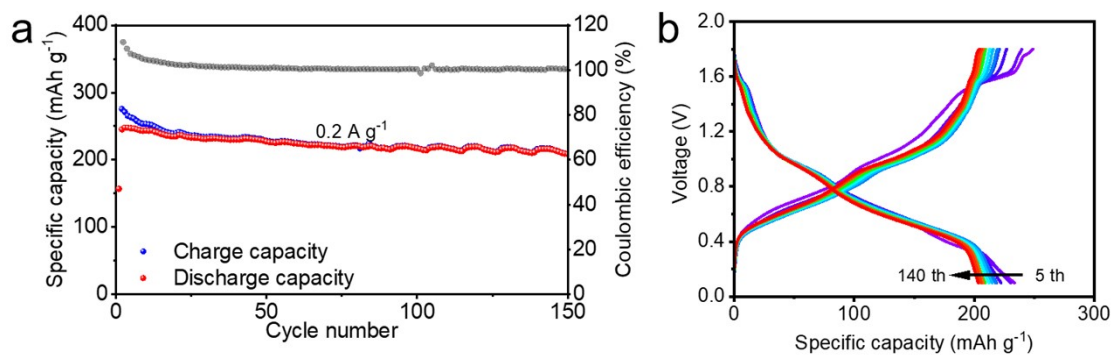


Figure S19. a) The electrochemical performance of VSSe electrode at the current density of 0.2 A g^{-1} and corresponding b) GCD curves from 5th to 140th.

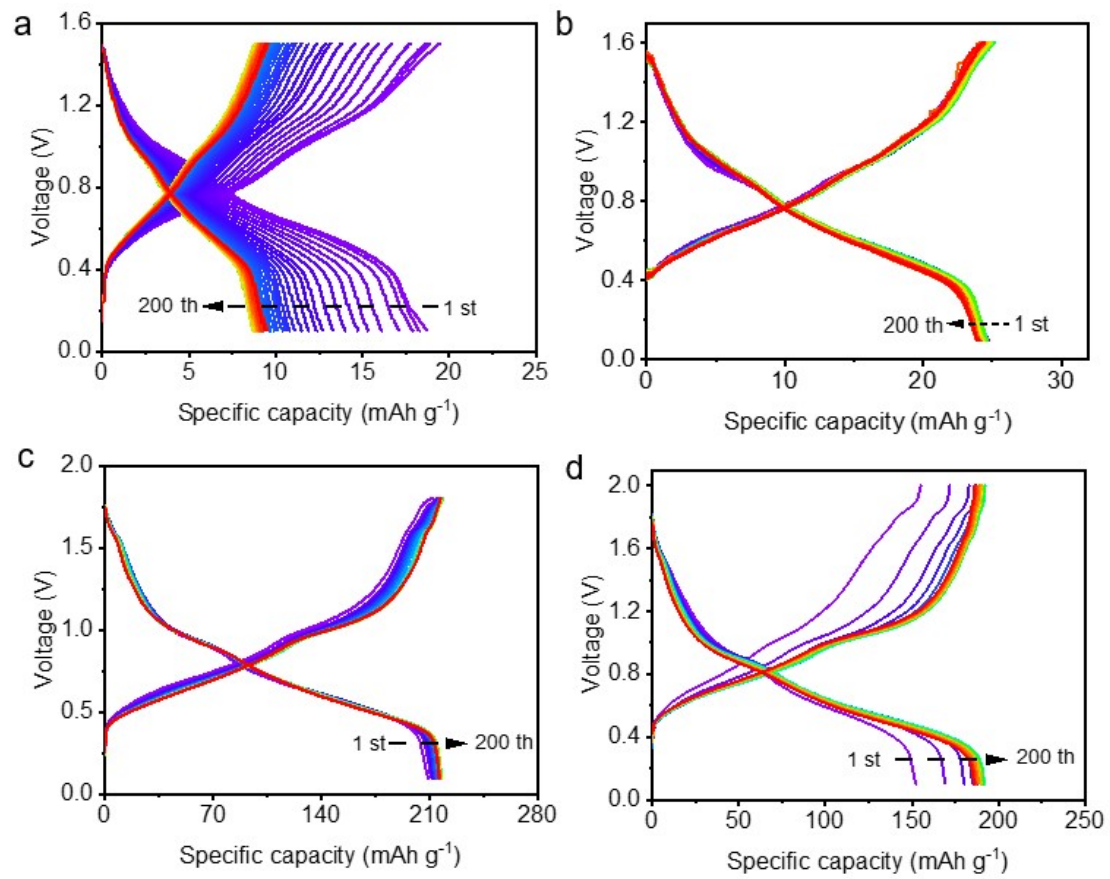


Figure S20. The galvanostatic charge-discharge (GCD) curves of VSSe electrodes with various voltage windows at current density of 1 A g^{-1} a) 0.1-1.5 V, b) 0.1-1.6 V, c) 0.1-1.8 V, and d) 0.1-2.0 V.

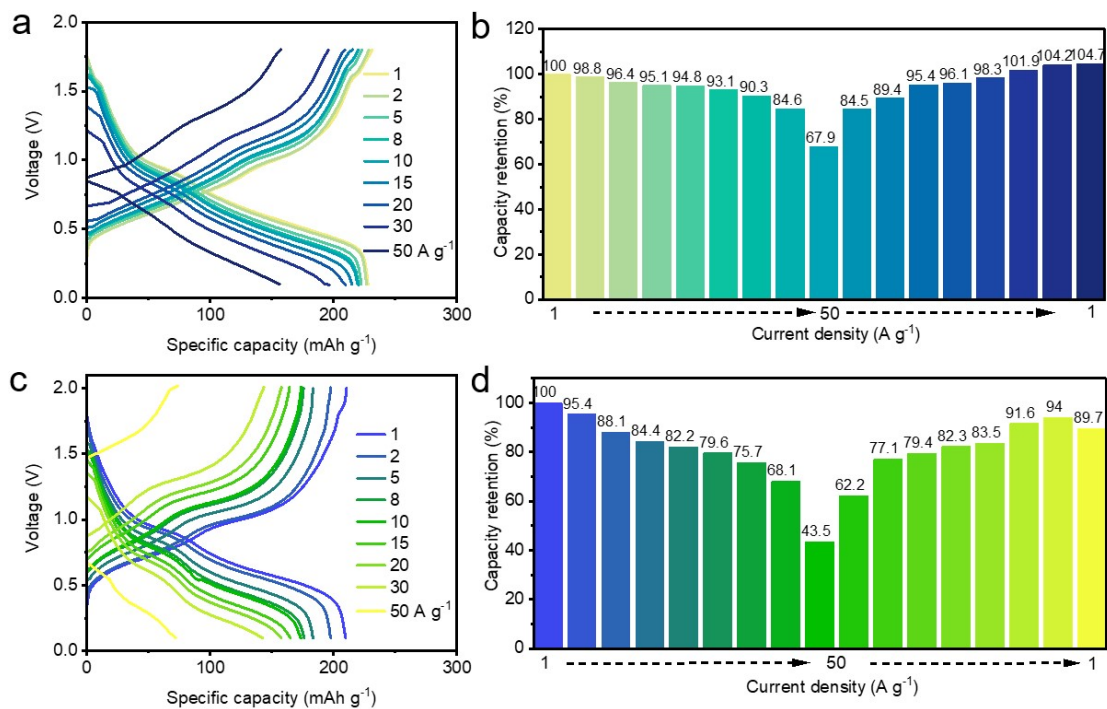


Figure S21. a) The GCD curves at 1, 2, 5, 8, 10, 15, 20, 30, 50 A g⁻¹, and corresponding (b) capacity retention of the VSSe electrode with the voltage window of 0.1-1.8 V. c) The GCD curves at 1, 2, 5, 8, 10, 15, 20, 30, 50 A g⁻¹, and corresponding d) capacity retention of the VSSe electrode with the voltage window of 0.1-2.0 V.

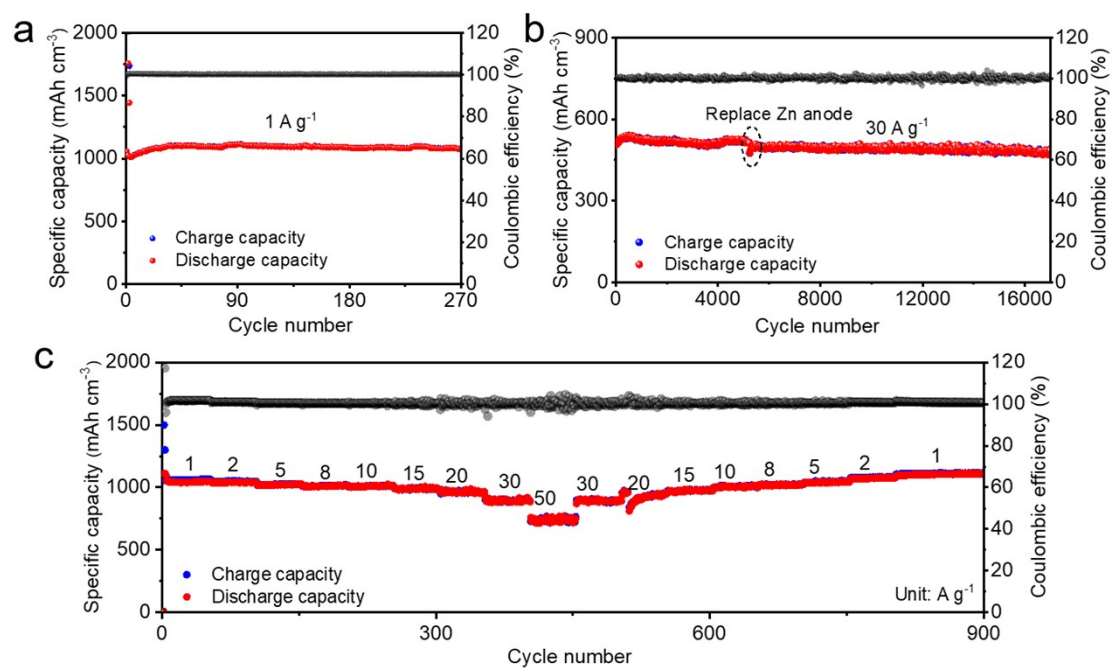


Figure S22 The electrochemical performance of the VSSe electrode with the voltage windows of 0.1-1.8 V in terms of volume capacity a) at 1 A g⁻¹, b) at 30 A g⁻¹, c) Rate performance.

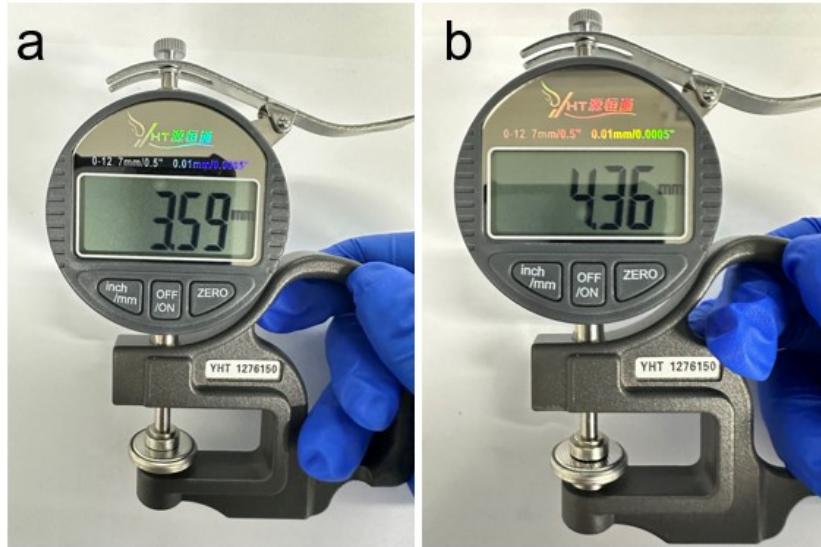


Figure S23. The thickness of cycled battery with the cut-off voltage of a) 1.8 V and b) 2.0 V.

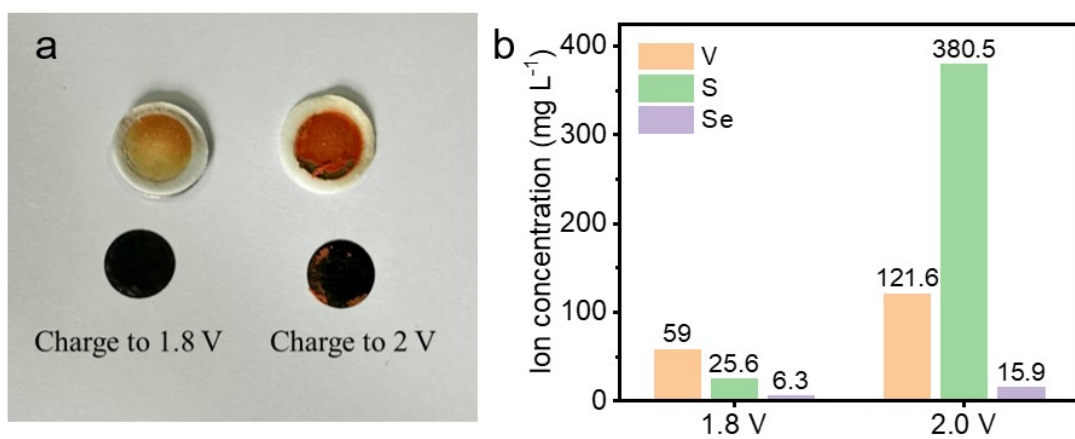


Figure S24. a) The digital images of batteries after 15000 cycles at 5 A g⁻¹ and corresponding b) ion dissolution with cut-off voltage of 1.8 V and 2.0 V.

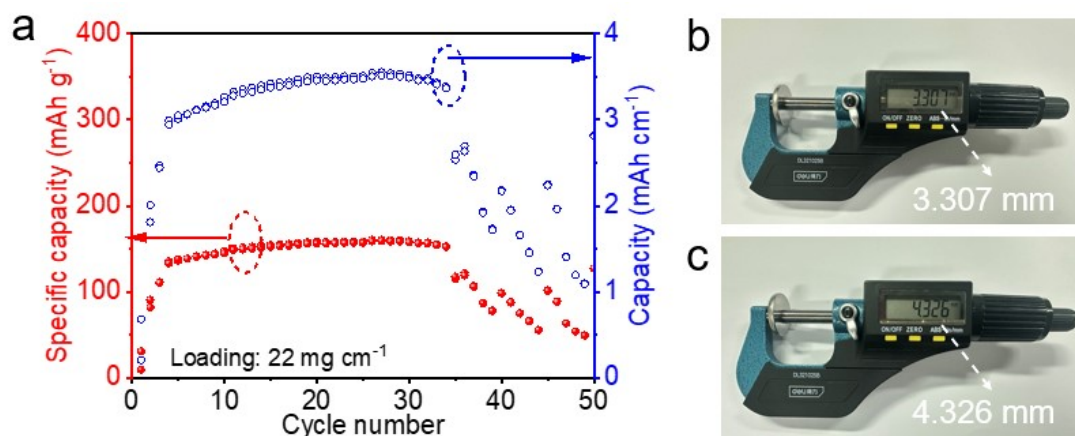


Figure S25. a) The cyclic performance of high-loading electrode at 0.1 A g⁻¹, b) the thickness of low-loading electrode after cycling 50 times, c) the thickness of high-loading electrode after cycling 50 times.

The high-loading electrode with 22.1 mg cm⁻¹ was further tested to assess the practicality, as depicted in **Figure S25**, it delivers an areal capacity of 3.51 mAh cm⁻² (mass specific capacity: 159 mAh g⁻¹) at the 27th cycle. However, the battery failed at the 35th cycle, which suggested that this battery should undergo more side-reactions, such as zinc corrosion and electrolyte decomposition according the thickness of cycled battery.

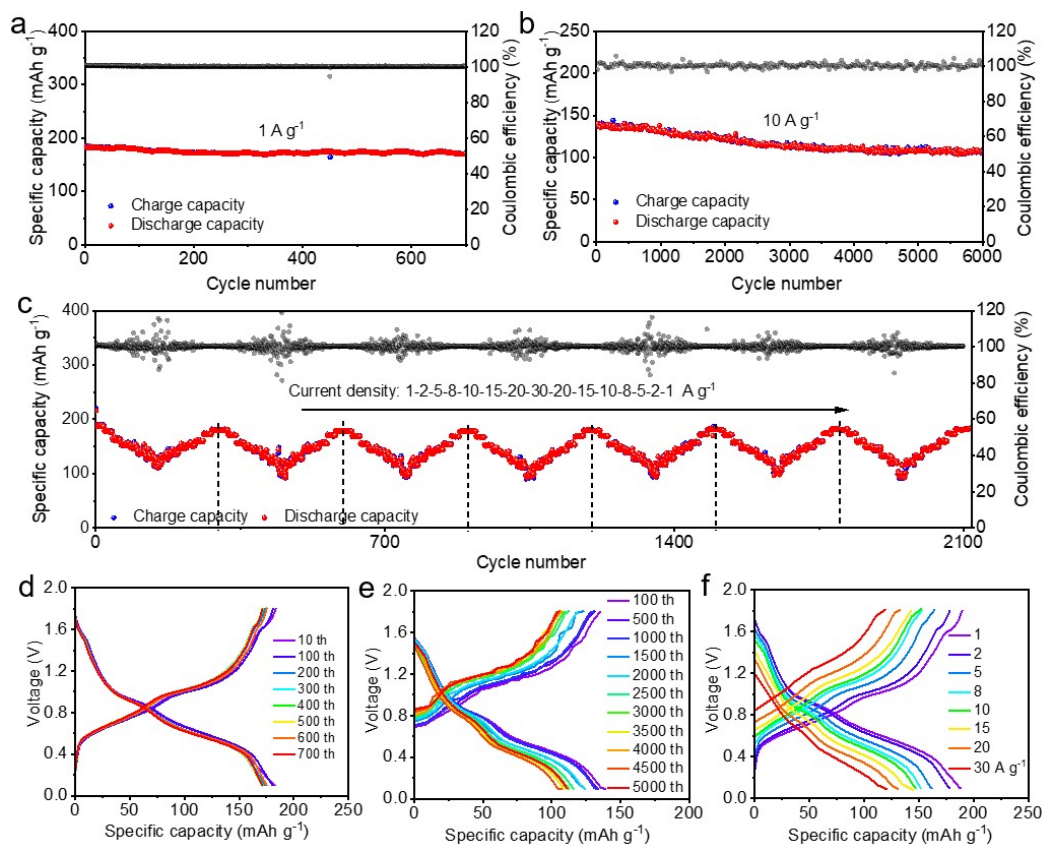


Figure S26. The electrochemical performance of VSSe electrode at low temperature a) The cyclic performance at current density of 1 A g^{-1} , b) The long cyclic performance at current density of 10 A g^{-1} , c) The rate performance from 1 A g^{-1} to 30 A g^{-1} for 7 rounds test. d) The GCD curves at 1 A g^{-1} from 10th to 700th. e) The GCD curves at 10 A g^{-1} from 100th to 5000th, and f) the GCD curves at 1st round rate cycling.

To show its fast kinetic in the low-temperature, the cycling performance and rate properties were measured at $0 \text{ }^\circ\text{C}$. It is seen that the prepared VSSe- V_2O_5 cathode not only provides high capacities of 170.6 mAh g^{-1} (capacity retention of 77.5%) at 1 A g^{-1} after 270 cycles, but also stable operates more than 700 cycles when the temperature decreases from $25 \text{ }^\circ\text{C}$ to $0 \text{ }^\circ\text{C}$. Similarly, high capacity of 107.1 mAh g^{-1} outstanding cycling performance (more than 6000 cycles) also maintain under a high current density of 10 A g^{-1} . What's more, the VSSe- V_2O_5 cathode delivers specific capacities of 190.0, 188.9, 178.3, 177.8, 163.9, 162.9, 154.4 and 152.8 mAh g^{-1} at current densities of 1, 2, 5, 8, 10, 15, 20, and 30 A g^{-1} , respectively, indicating that the VSSe- V_2O_5 cathode also possesses remarkable rate performance at low-temperature. Notably, the GCD plots show a similar shape compared with the results measured at $25 \text{ }^\circ\text{C}$ and highly overlap after different cycles, indicating its fast kinetic of proposed VSSe- V_2O_5 cathode in AZIBs even at low-temperature.

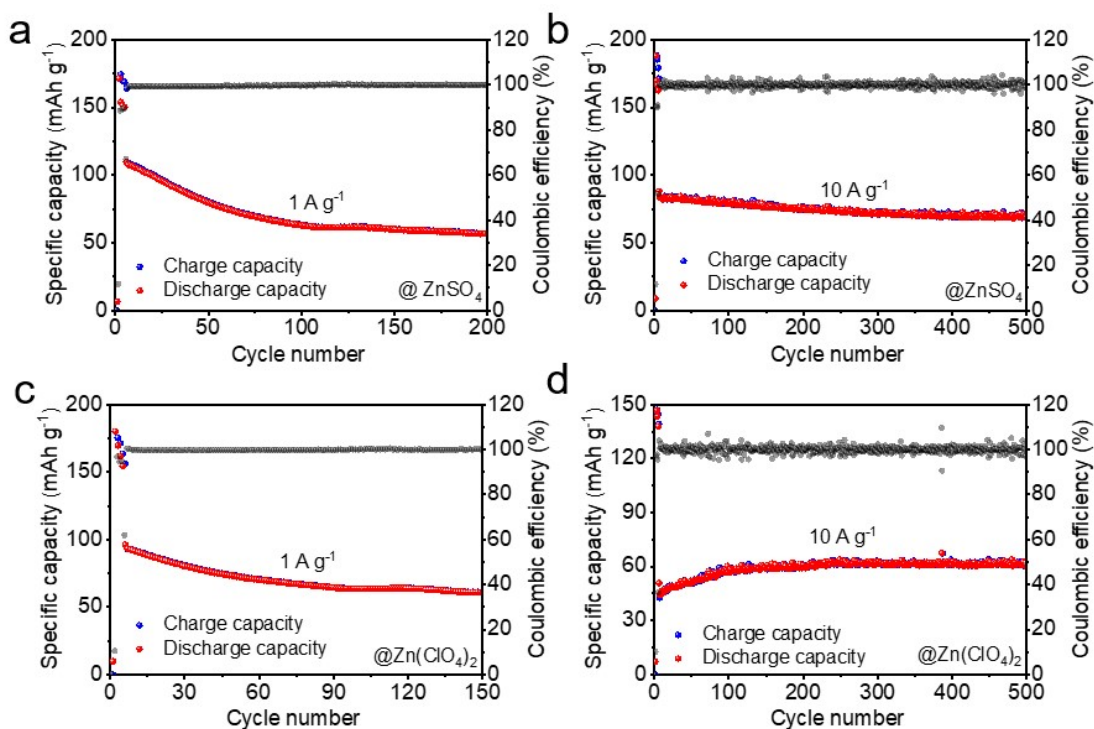


Figure S27. The electrochemical performance of VSSe electrode with 3M ZnSO_4 electrolyte a) 1 A g^{-1} , b) 10 A g^{-1} , and with 3M $\text{Zn}(\text{ClO}_4)_2$ electrolyte c) 1 A g^{-1} , d) 10 A g^{-1} .

To investigate the influence of different electrolytes on the customized crystalline-amorphous heterojunction of VSSe electrode, the corresponding electrochemical cycling performance were tested, as shown in **Figure S27**. At a current density of 1 A g^{-1} , VSSe electrode exhibited a rapid decay trend in both ZnSO_4 and $\text{Zn}(\text{ClO}_4)_2$ electrolytes. After 150 cycles, the specific capacity was only 60 mAh g^{-1} and 61 mAh g^{-1} , respectively. However, at a current density of 10 A g^{-1} , although the specific capacity remained relatively stable, the capacity was still lower than that in $\text{Zn}(\text{CF}_3\text{SO}_3)_2$ electrolyte.

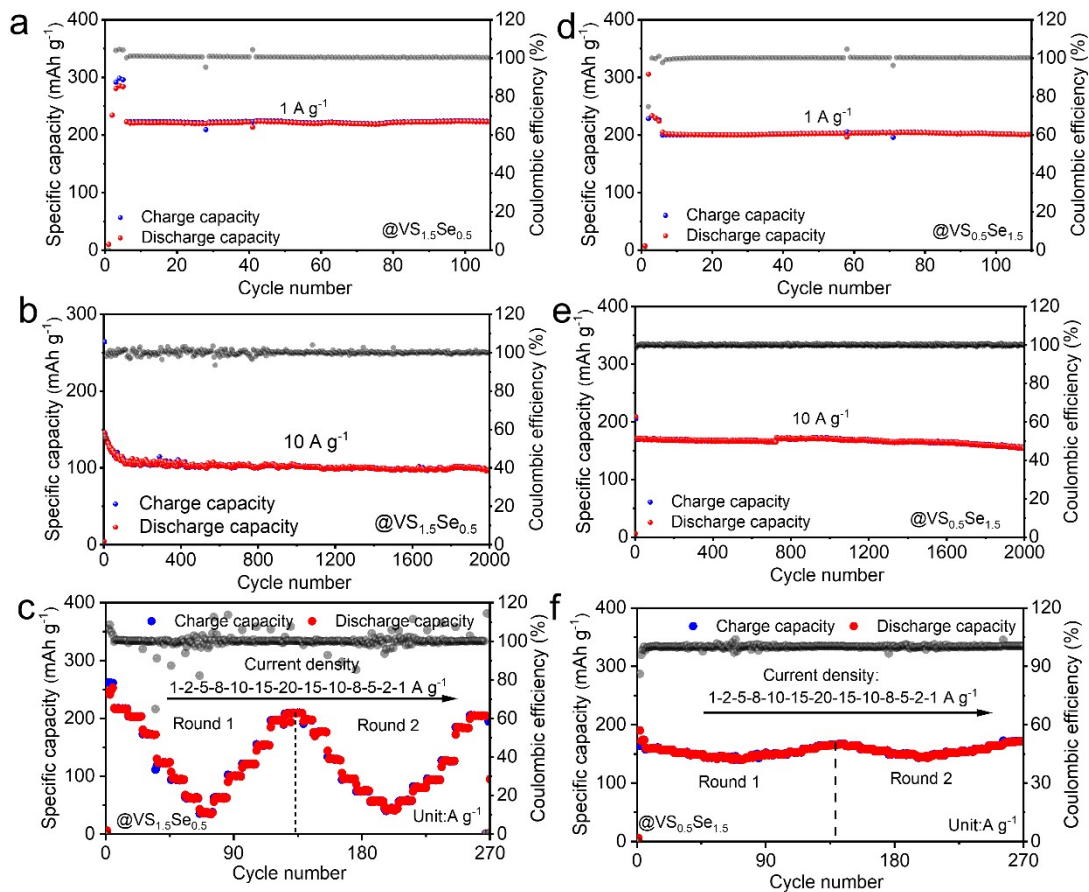


Figure S28. The electrochemical performance of $\text{VS}_{1.5}\text{Se}_{0.5}$ a) at 1 A g^{-1} , b) 10 A g^{-1} and c) Rate capacity from 1 A g^{-1} to 20 A g^{-1} . The electrochemical performance of $\text{VS}_{0.5}\text{Se}_{1.5}$ d) at 1 A g^{-1} , e) 10 A g^{-1} and f) Rate capacity from 1 A g^{-1} to 20 A g^{-1} .

The obtained $\text{VS}_{1.5}\text{Se}_{0.5}$ and $\text{VS}_{0.5}\text{Se}_{1.5}$ materials are also applied as cathode to assemble zinc ion battery, the tests were conducted on 1A, 10A and rate cycling. Among them, $\text{VS}_{1.5}\text{Se}_{0.5}$ and $\text{VS}_{0.5}\text{Se}_{1.5}$ showed capacities of 223 mAh g^{-1} and 201 mAh g^{-1} respectively at a current density of 1 A g^{-1} , and capacities of 96 mAh g^{-1} and 154 mAh g^{-1} after 2000 cycles at a current density of 10 A g^{-1} . Besides, $\text{VS}_{0.5}\text{Se}_{1.5}$ demonstrated superior rate performance. Thus, it can be inferred that as the Se content increases, the specific capacity becomes relatively lower, but it has better rate performance.

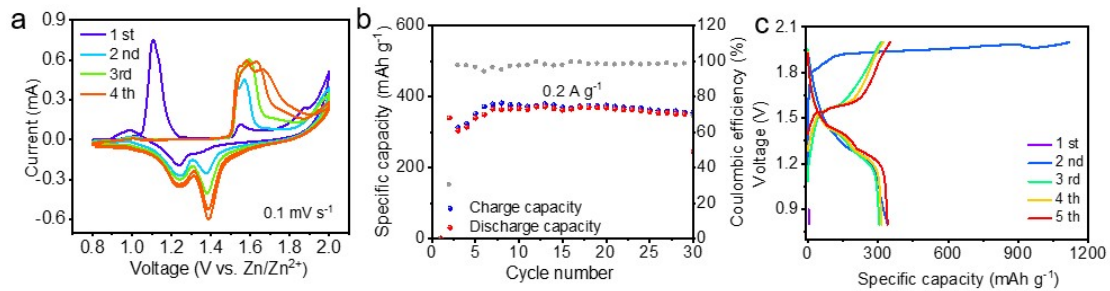


Figure S29. a) The first 4th CV profiles of MnS_{0.5}Se_{0.5} cathode at 0.1 mV s⁻¹, b) the cyclic performance at 0.2 A g⁻¹ and corresponding c) GCD curves from 1st to 5th.

When MnS_{0.5}Se_{0.5} is directly used as the positive electrode of zinc-ion battery, the evolution of CV peaks shows a phase transformation process similar to that of VSSe. After the phase transformation, it exhibits a high specific capacity of 379 mAh g⁻¹ at a current density of 0.2 A g⁻¹. The GCD graph shows that VSSe undergoes electrochemical activation in the first cycle and then presents a charge-discharge curve similar to that of MnO_x.

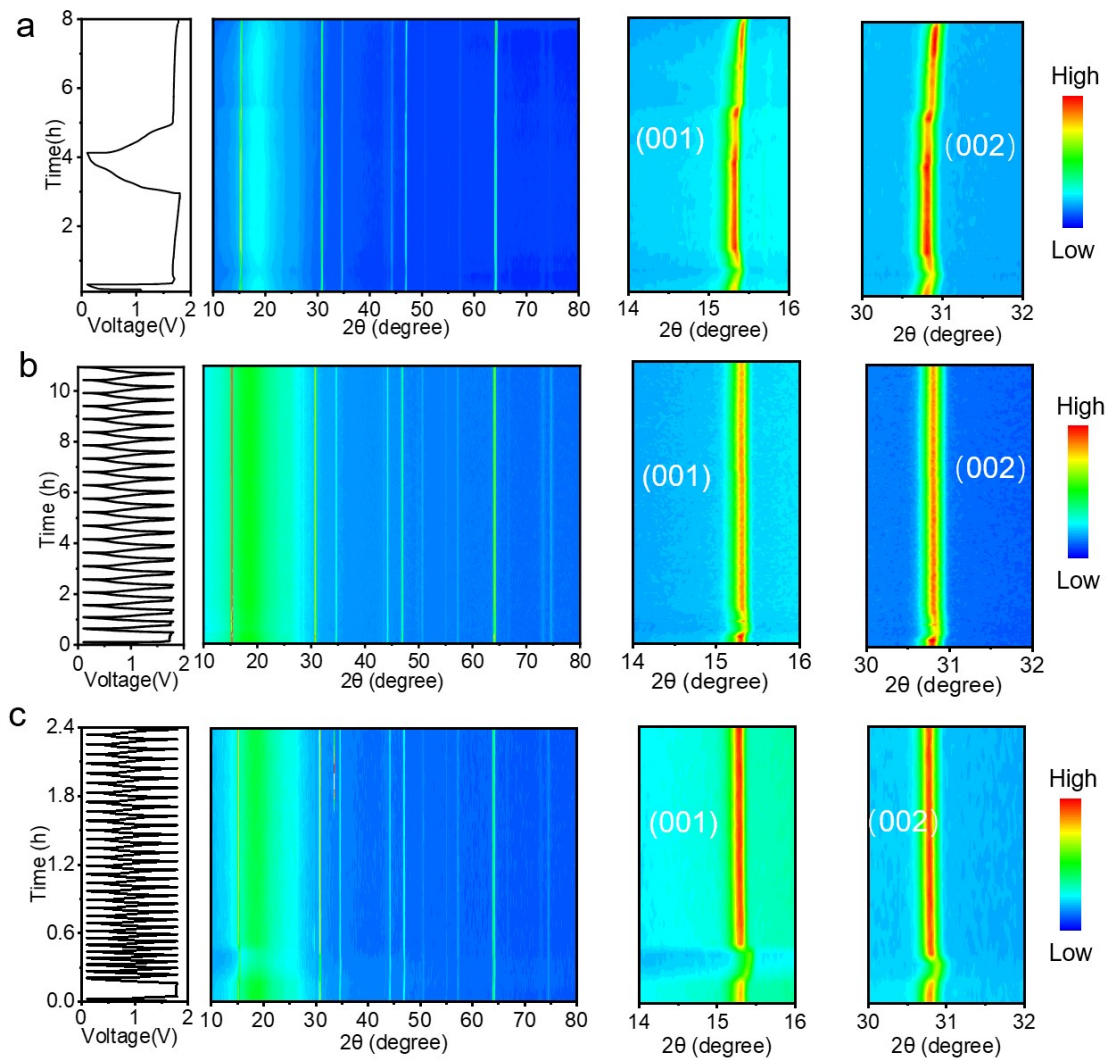


Figure S30. The *in-situ* XRD patterns of VSSe electrodes with 3M $\text{Zn}(\text{CF}_3\text{SO}_3)_2$ electrolyte at various current densities a) 0.1 A g^{-1} , b) 0.5 A g^{-1} and c) 1 A g^{-1} .

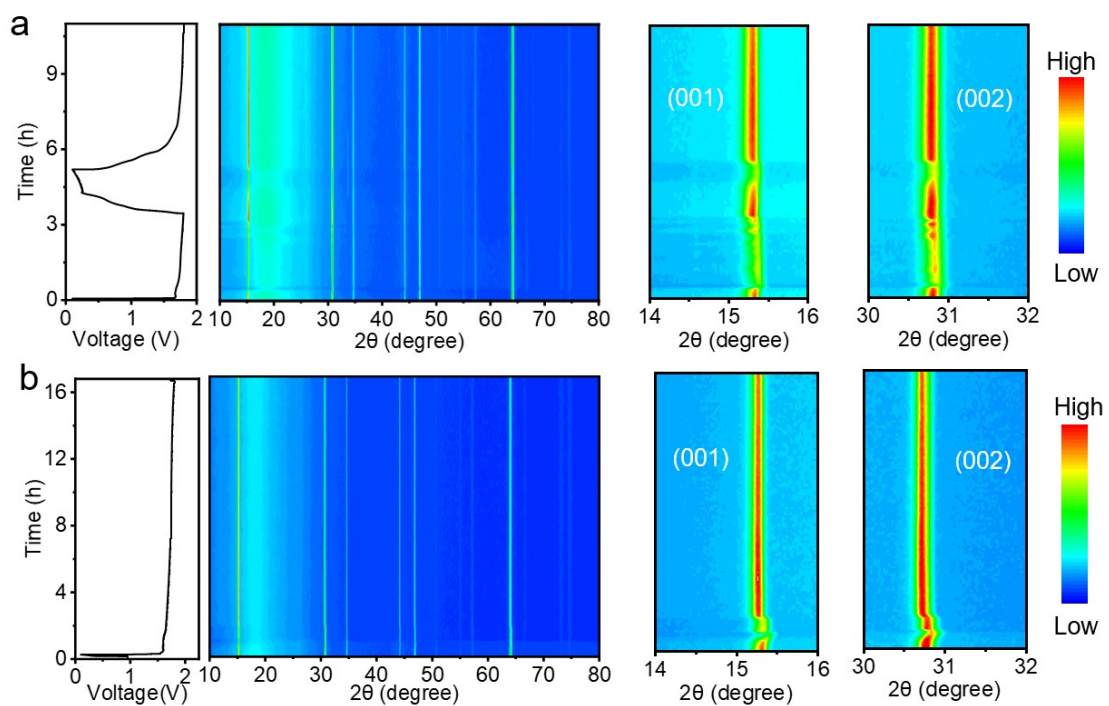


Figure S31. The in-situ XRD patterns of VSSe electrodes with others electrolyte at a current density of 0.1 A g⁻¹, a) 3M ZnSO₄ electrolyte, and c) 3M Zn(ClO₄)₂ electrolyte.

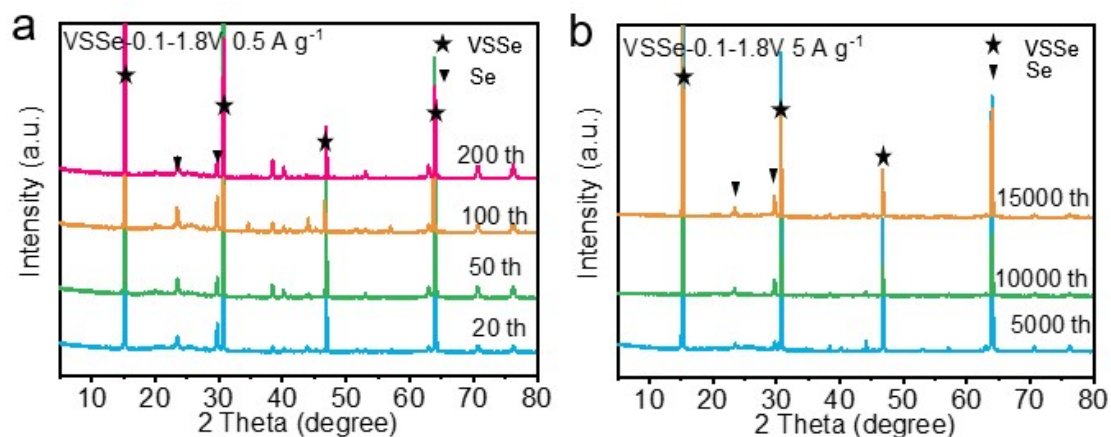


Figure S32. (a) The XRD curves of VSSe cathode after 20, 50, 100 and 200 cycles at 0.5 A g^{-1} . (b) The XRD curves of VSSe cathode after 5000, 10000 and 15000 cycles at 5 A g^{-1} .

XRD curves of the electrode cycled at different current densities (0.5 A g^{-1} and 5 A g^{-1}) at a cutoff voltage of 1.8 V for different cycles. It can be observed that the characteristic peaks of VSSe remain present after cycled for 20, 50, 100, and 200 cycles at 0.5 A g^{-1} , even at a high current density of 5 A g^{-1} after 5000, 10000, and 15000 cycles.

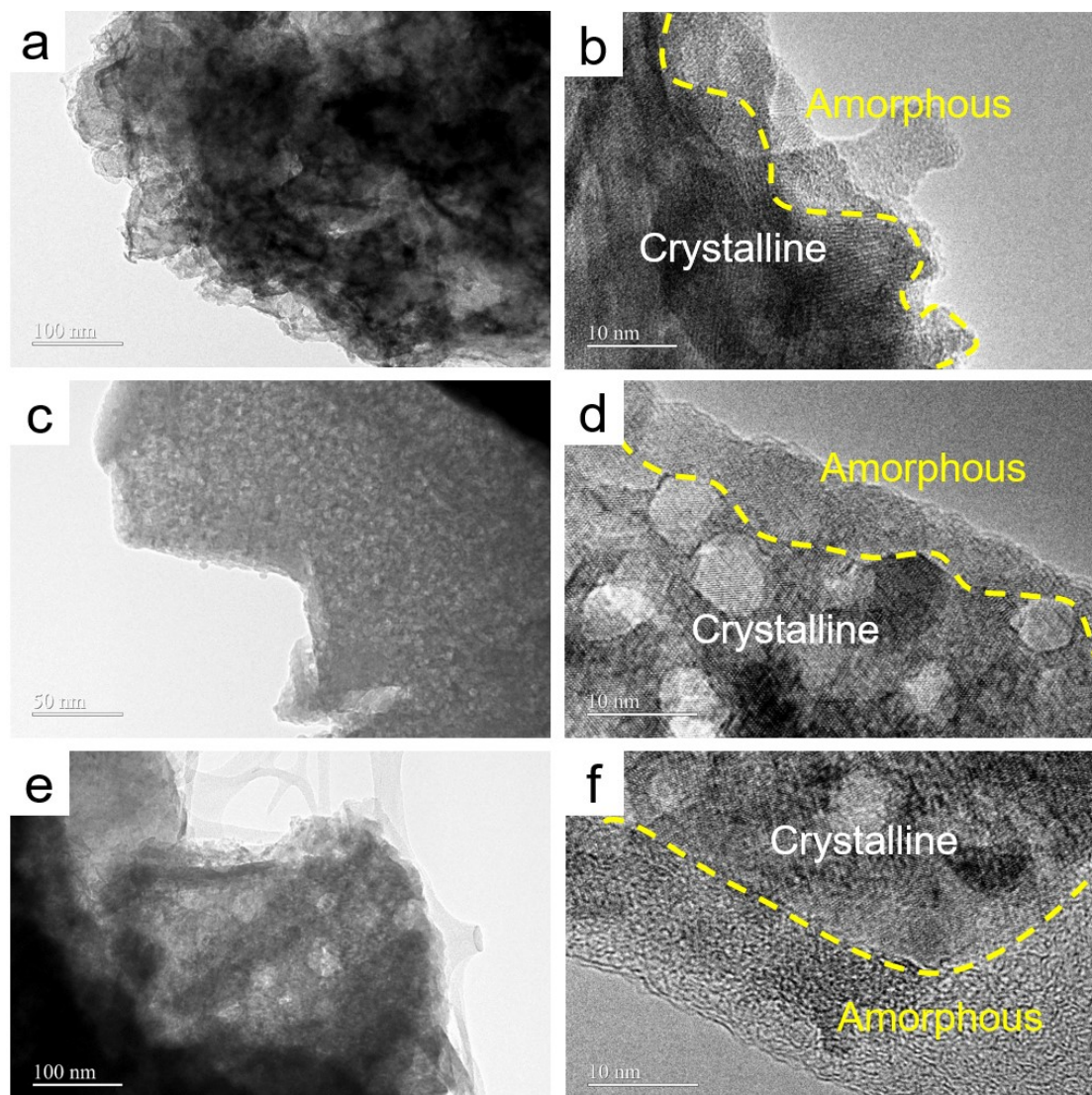


Figure S33. The TEM images of VSSe material cycled at 0.5 A g^{-1} for (a, b) 20th, (c, d) 50th and (e, f) 100th.

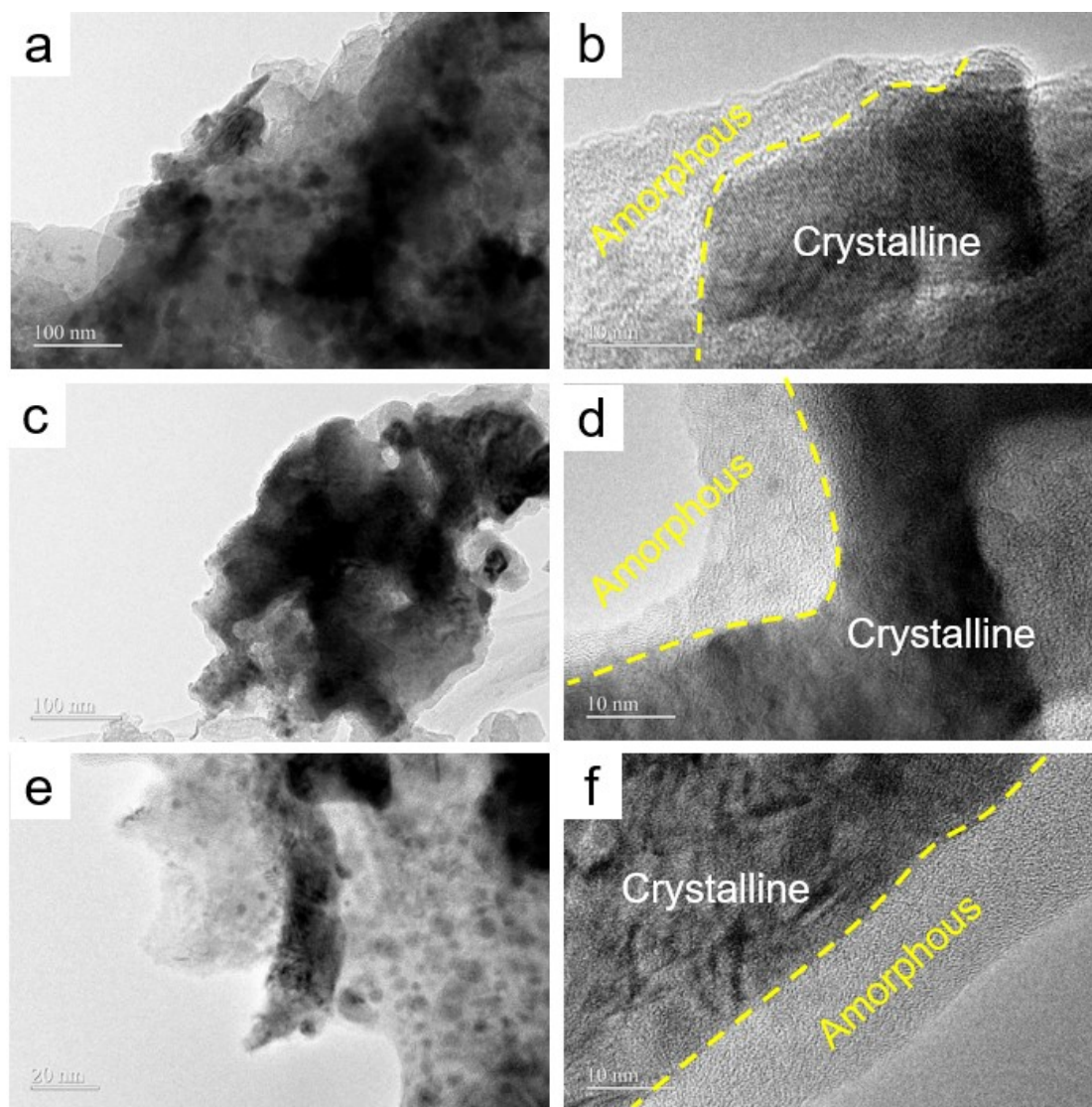


Figure S34. The TEM images of VSSe material cycled at 5 A g^{-1} for (a, b) 5000th, (c, d) 10000th and (e, f) 15000th.

To investigate the stability of the heterojunction structure, TEM characterization was conducted on electrodes after different cycles. The electrode material still remains crystalline-amorphous heterojunction architecture after charged/discharged 20, 50 and 100 cycles at 0.5 A g^{-1} , as clearly shown in **Figure S33**. The TEM characterization was also performed after cycled 5000, 10000 and 15000 times at a high current density of 5 A g^{-1} (**Figure S34**), which also exhibit crystalline-amorphous heterojunction architecture.

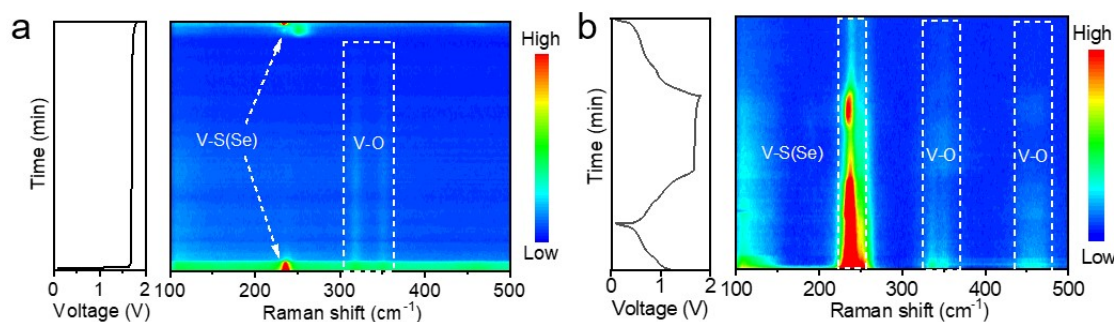


Figure S35. In-situ Raman Spectroscopy of the VSSe electrode. a) First Cycle, b) Second Cycle.

To better understand the correlation between its electrochemical performance and structure, we conducted *in-situ* Raman spectroscopy on the VSSe-V₂O₅ heterojunction. **Figure S35a** presents the *in-situ* Raman spectra during the first cycle. It can be observed that the vibrational peak of the V-S/Se bond at 236.1 cm⁻¹ disappears during the initial discharge and upon charging to 1.6 V. During the subsequent charging process, an E_{2g} vibrational peak of V-S/Se emerges at 250 cm⁻¹ at approximately 1.8 V, followed by the appearance of a V-O vibrational peak at 318 and 352 cm⁻¹. This indicates that the V-S bond breaks, leading to the formation of V₂O₅. Finally, upon charging to 1.8 V, the vibrational peak around 236.18 cm⁻¹ can be attributed to the coexistence of V-O, V-S, and V-S/Se bonds, confirming the formation of the VSSe/V₂O₅ heterojunction. To verify the stability of the heterojunction during subsequent cycles, Figure S presents the in-situ Raman spectra of the second cycle. It can be observed that the coexistence of the three bonds persists; however, during charging, the peak intensity gradually decreases. This may be due to the continuous transformation of some V-S/Se bonds into V=O, leading to the complete coverage of VSSe by amorphous V₂O₅, which weakens the V-S/Se vibrational peaks.

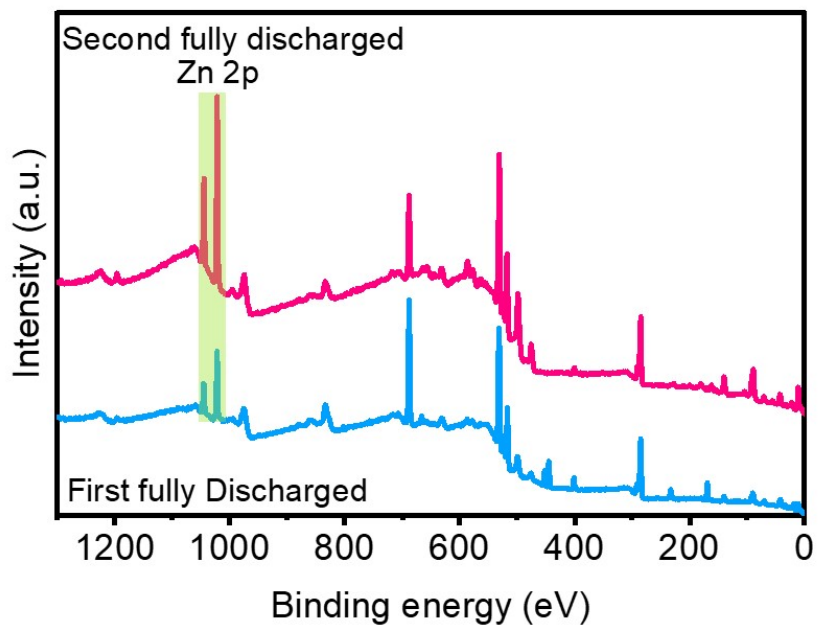


Figure S36. The ex-situ XPS survey spectra of VSSe electrode (charged to 1.8 V) at first and second fully discharged state.

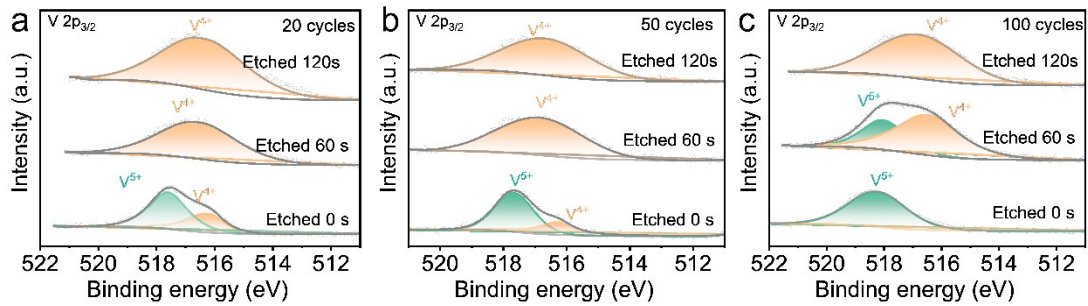


Figure S37. The XPS spectrums of V $2p_{3/2}$ etched 0, 60 and 120 s after cycled a) 5000, b) 10000, c) 15000 times.

As shown in the **Figure S37**, after 20 cycles, the electrode surface exhibits a coexistence of V^{5+} and V^{4+} . After etching 60s and 120s, the proportion of V^{4+} gradually increases until V^{5+} disappears, indicating the coexistence of V_2O_5 and VSSe on the electrode surface. After 50 cycles, the surface still shows the coexistence of V^{5+} and V^{4+} . A half quantitative analysis of different valence states of V ions reveals that the proportion of V_2O_5 increases at this stage. Upon etching 60s and 120s, V^{4+} content increases, and V^{5+} eventually disappears. After 100 cycles, the electrode surface predominantly consists of V^{5+} , indicating that V_2O_5 continues to generate and gradually covers the electrode surface during cycle. V^{4+} reappears after etching, suggesting that VSSe remains stable within the electrode bulk. Combined with the long-cycle stability shown in **Figure 3**, these results confirm that the VSSe- V_2O_5 electrode maintains a stable crystalline-amorphous dynamic equilibrium throughout prolonged cycling.

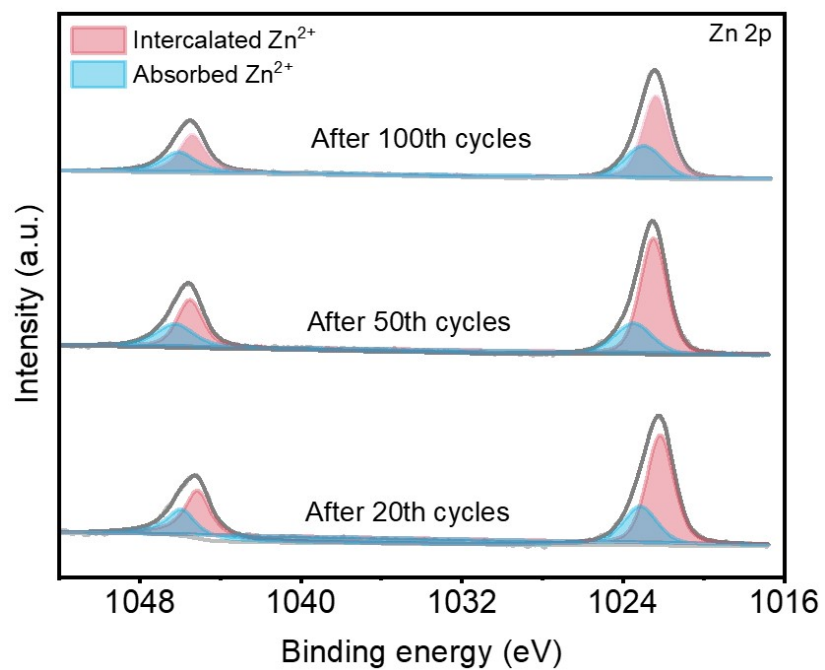


Figure S38. The ex-situ Zn 2p XPS spectra of VSSe electrode at 1.8 V for cycling 20th, 50th and 100th.

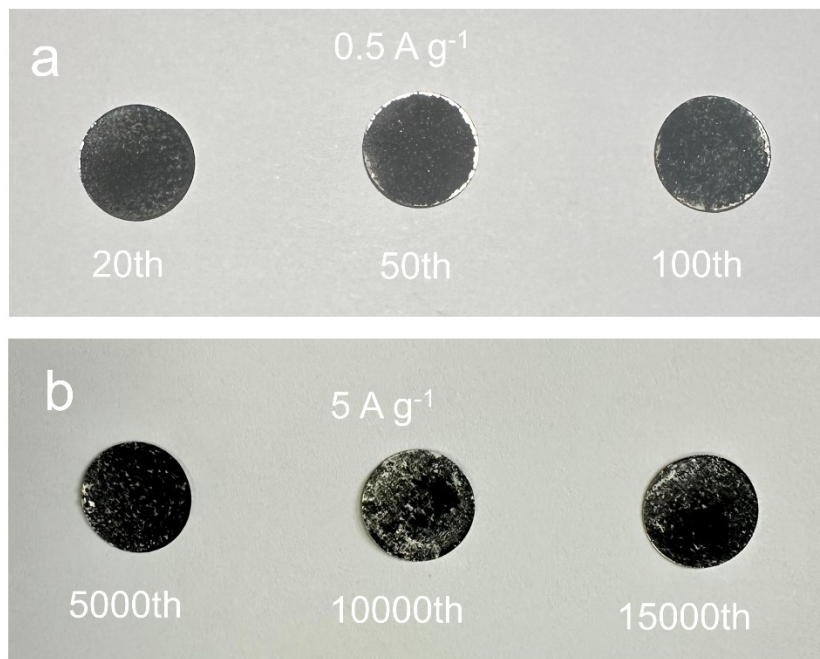


Figure S39. The digital images of VSSe-V₂O₅ electrodes a) at 0.5 A g⁻¹ after 20, 50 and 100 cycles, b) at 5 A g⁻¹ after 5000, 10000 and 15000 cycles.

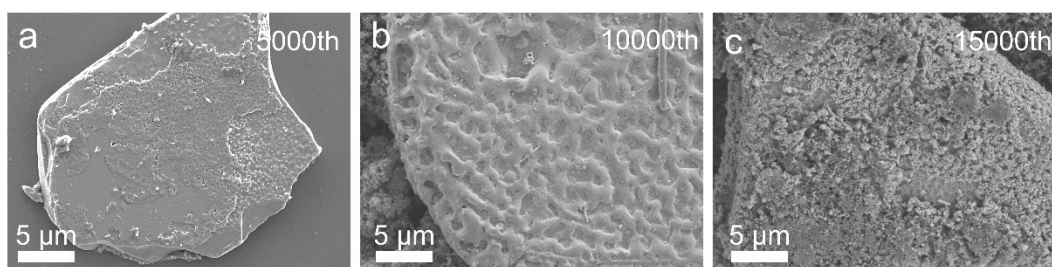


Figure S40. The SEM images of VSSe-V₂O₅ electrodes at 5 A g⁻¹ after a) 5000, b) 10000 and c) 15000 cycles.

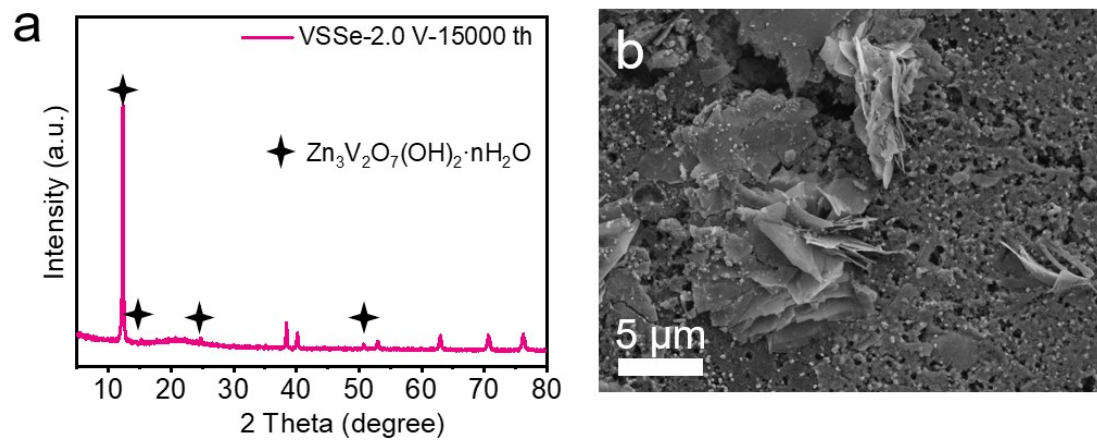


Figure S41. a) The XRD pattern and b) SEM image of VSSe electrode charging to 2.0 V after 15000 cycles at 5 A g⁻¹.

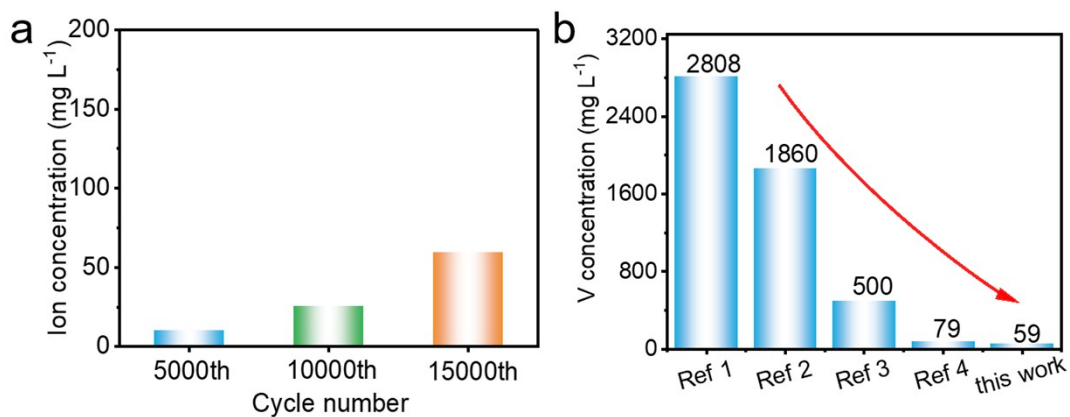


Figure S42. a) The vanadium dissolution after 5000, 10000 and 15000 cycles, b) The comparison of vanadium dissolution with reported V-based materials after cycling.

To investigate solubility of V, the V-dissolution content in VSSe-V₂O₅ cathode were characterized by the ICP after cycled for 5000, 10000 and 15000 cycles (**Figure S42a**) and compared with reported V-based materials (**Figure S42b**) It seen that the V-dissolution content in our designed VSSe-V₂O₅ cathode is less than those of previous reports, contributing to better electrochemical performance for the VSSe-V₂O₅ cathode.

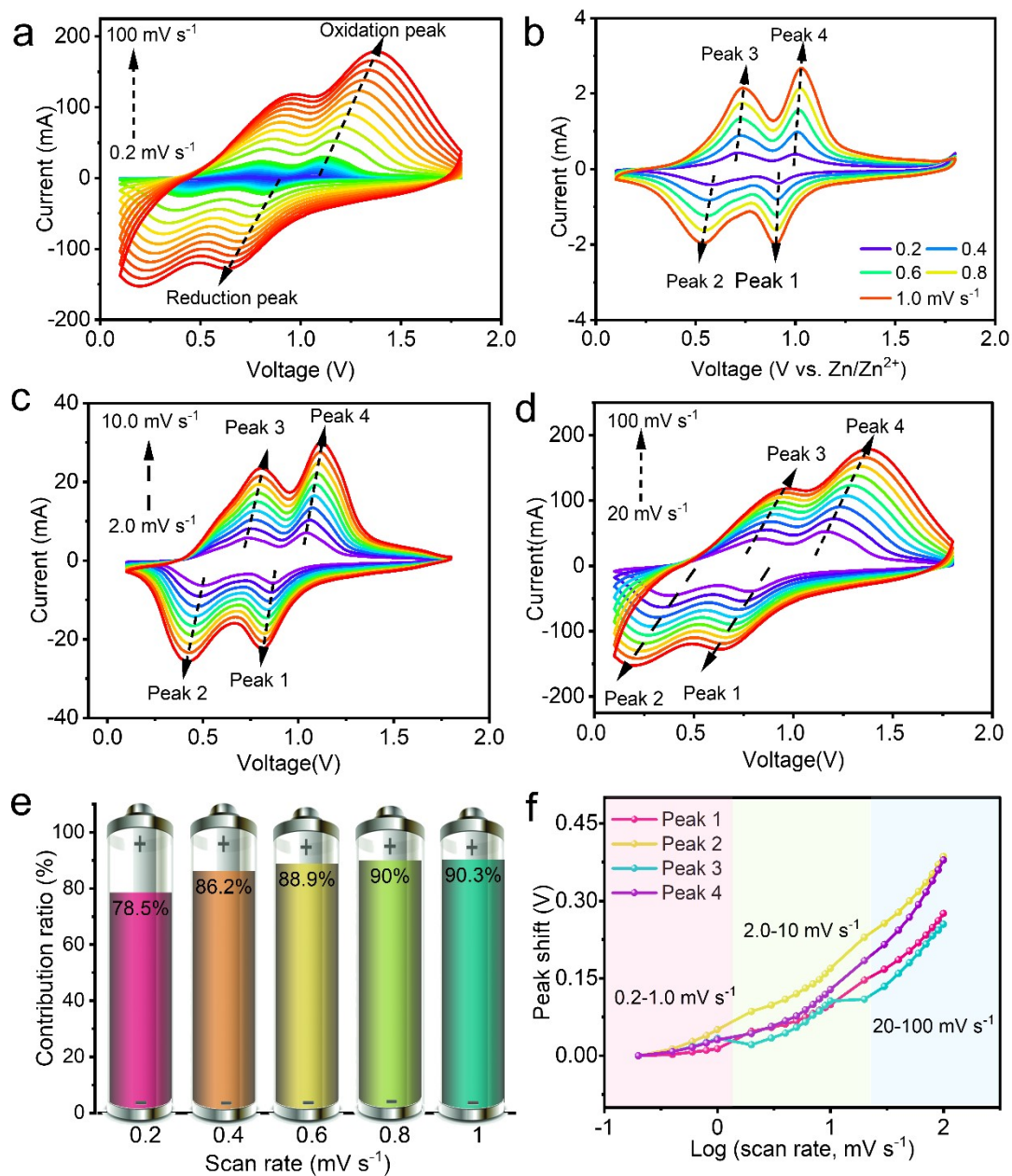


Figure S43. CV curves of Zn/VSSe-V₂O₅ batteries at different scan rates. a) from 0.2 to 100 mV s⁻¹, b) from 0.2 to 1 mV s⁻¹, c) from 2 to 10 mV s⁻¹, d) from 20 to 100 mV s⁻¹. e) Capacitive and diffusion-controlled capacity contribution at scan rates of 0.2-1.0 mV s⁻¹. f) The correlation of the cathodic and anodic peak potential shifts with the scan rates.

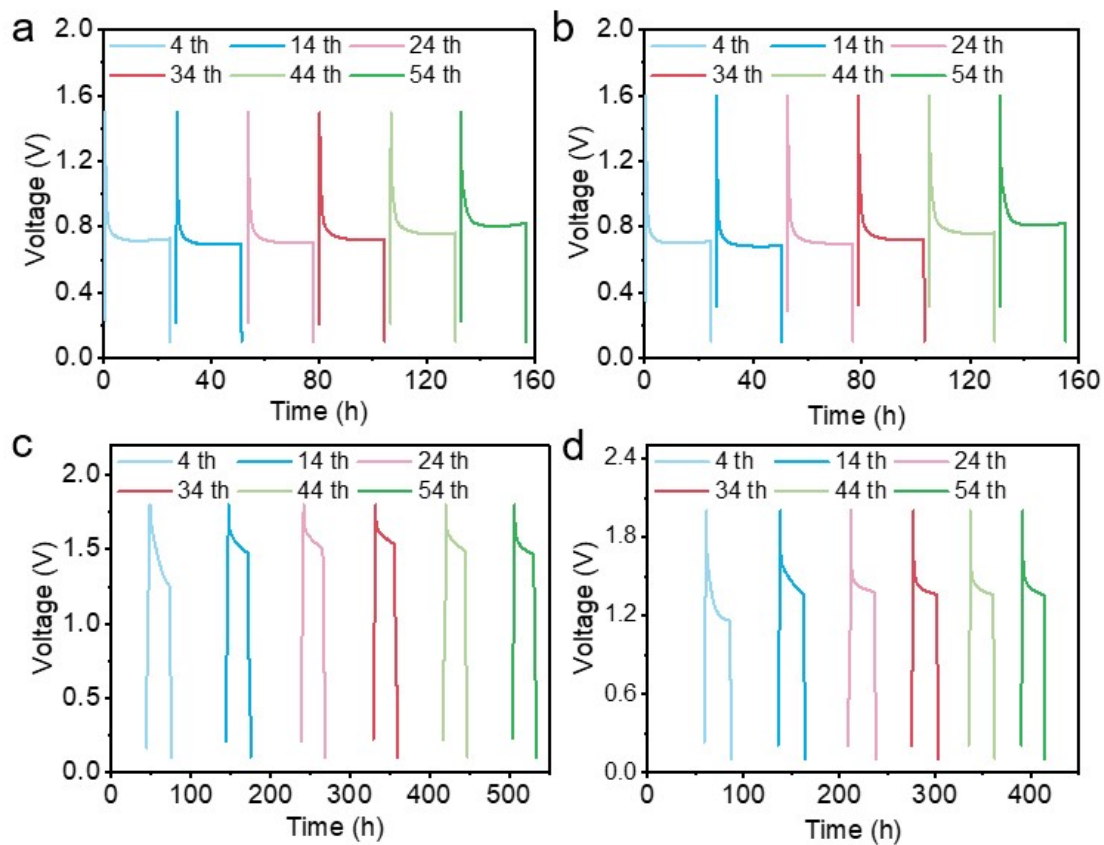


Figure S44. The self-discharge curves at 4th, 14th, 24th, 34th, 44th and 54th with cut-off voltage of a) 1.5 V, b) 1.6 V, c) 1.8 V and d) 2.0 V.

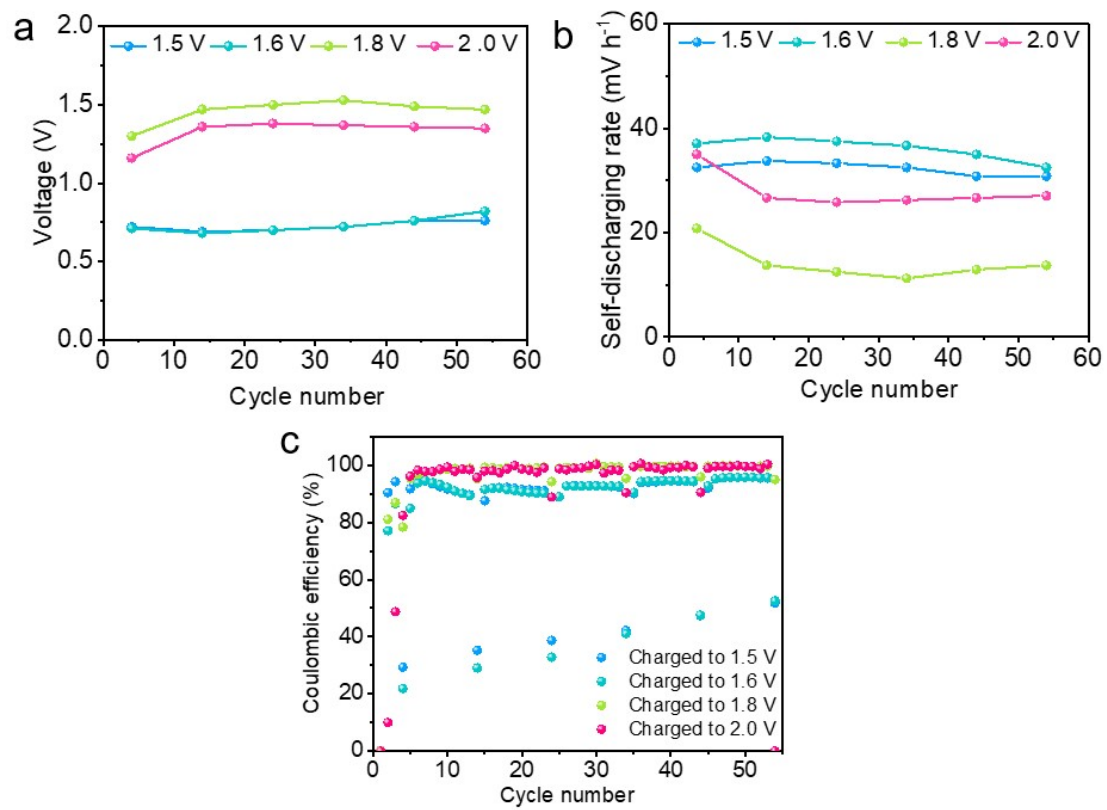


Figure S45. a) The remained voltages and b) The self-discharging rate variation, c) The coulombic efficiency from 4th to 54th with different cut-off voltages cycling.

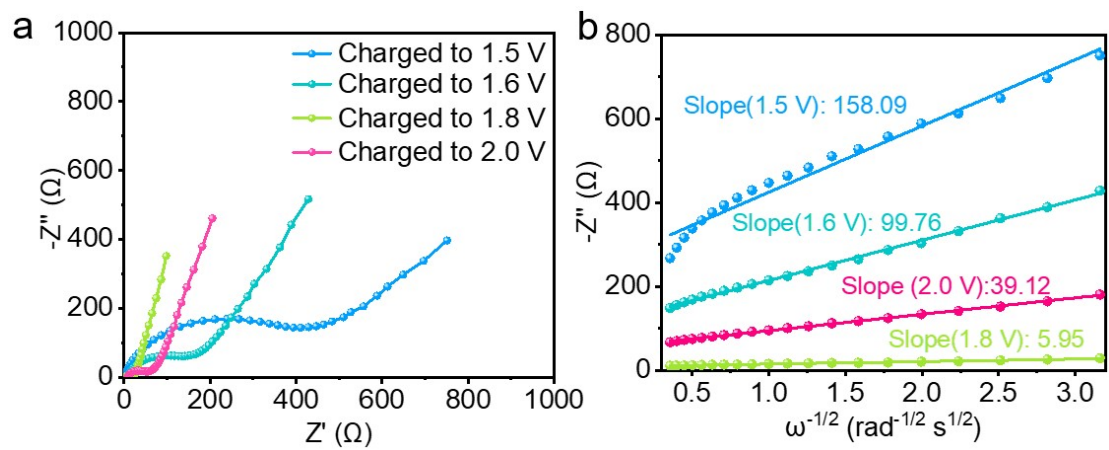


Figure S46. a) The EIS curves, and b) corresponding diffusion coefficient of VSSe electrode with cut-off voltages.

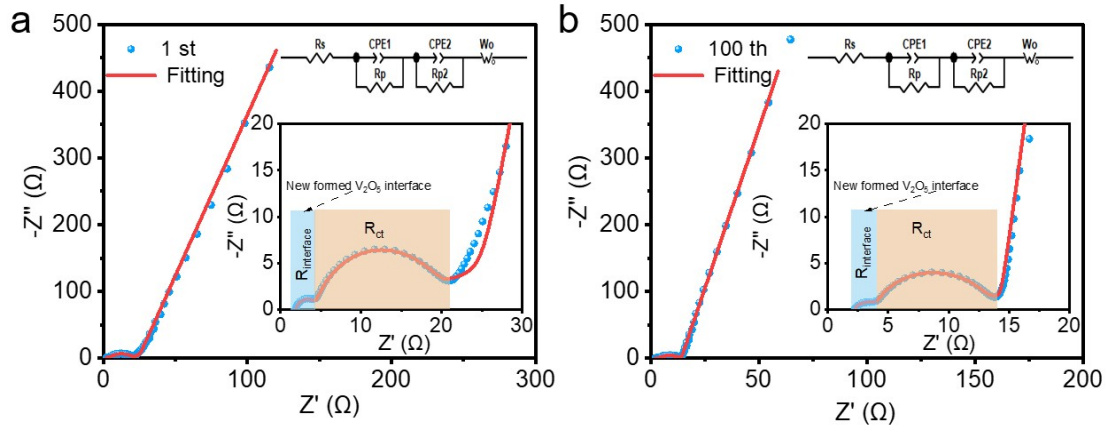


Figure S47. Nyquist plots of the battery and the corresponding fitting results (the inset shows the equivalent circuit) a) 1st cycle, and b) 100th cycle.

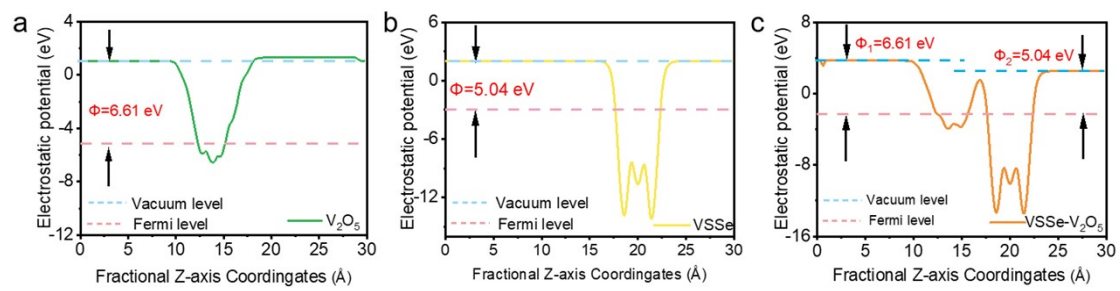


Figure S48. The work function curves of a) V_2O_5 , b) VSSe, and c) VSSe- V_2O_5 .

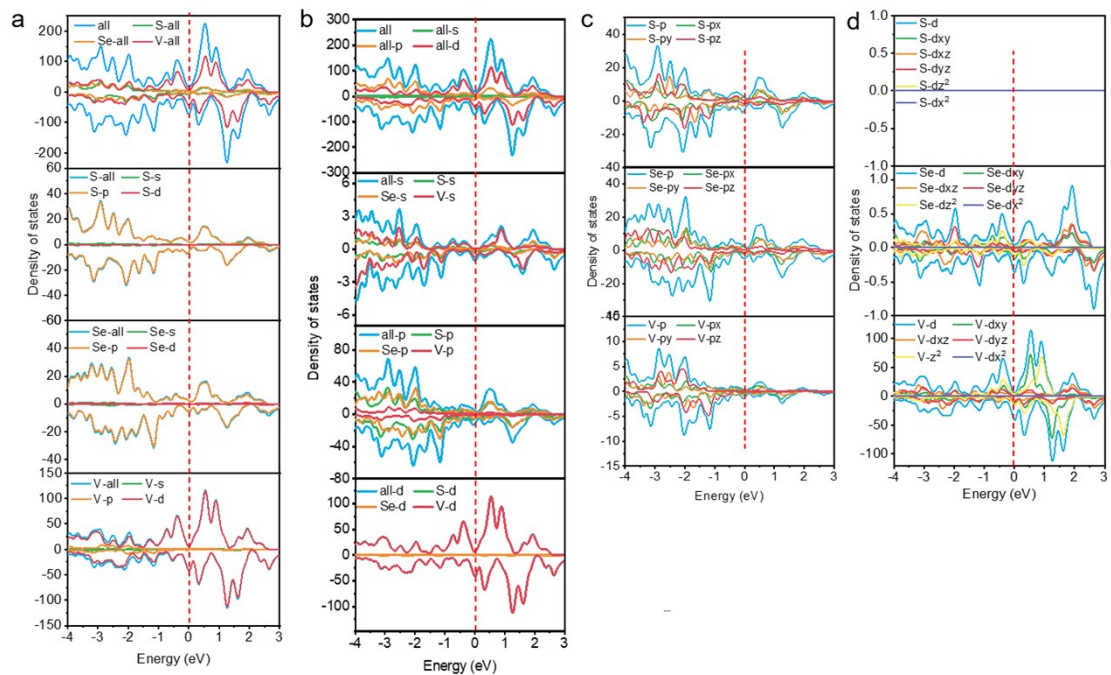


Figure S49. The DOS of VSSe material. a) The TDOS and PDOS of V, S and Se element, b) the all and s, p and d orbitals DOS curves, c) the p orbital DOS curves and d) the d orbital DOS curves.

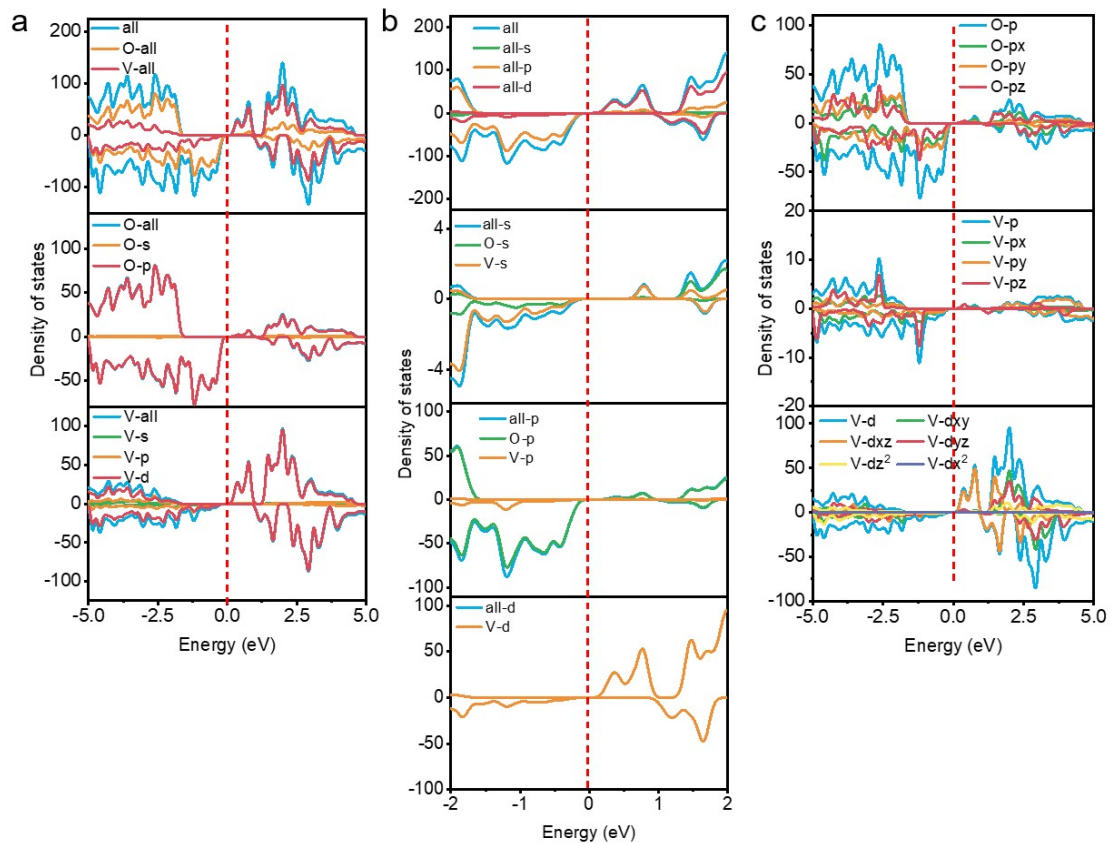


Figure S50. The DOS of V_2O_5 material. a) The TDOS and PDOS of V and O element, b) the all and s, p and d orbitals DOS curves, c) the p and d orbital DOS curves.

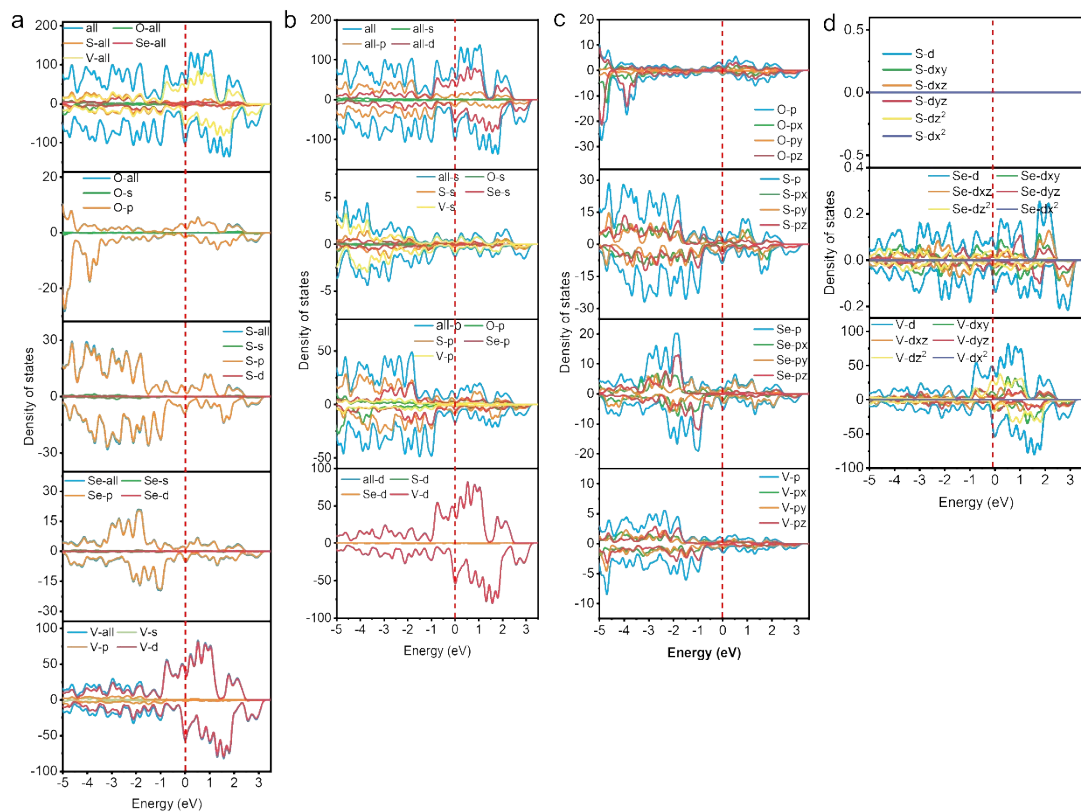


Figure S51. The DOS of VSSe-V₂O₅ material. a) The TDOS and PDOS of V, S, Se and O element, b) the all and s, p and d orbitals DOS curves, c) the p orbital DOS curves and d) the d orbital DOS curves.

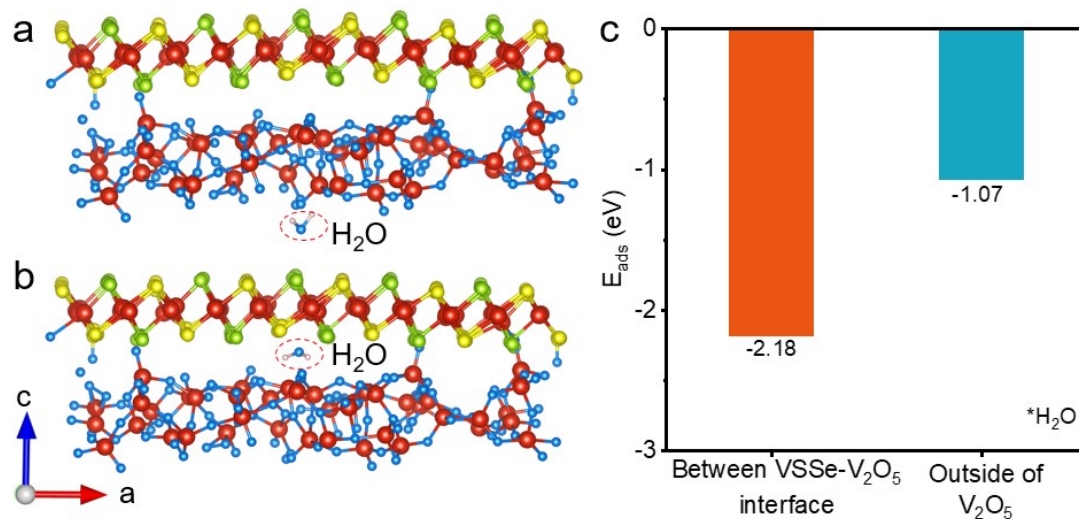


Figure S52. a) The adsorption structure for H₂O at outside of V₂O₅, b) The adsorption structure for H₂O at VSSe- V₂O₅ interface, c) The adsorption energy for H₂O at outside of V₂O₅ and VSSe- V₂O₅ interface.

specific capacity. Conversely, VS_2 exhibits a relatively higher theoretical specific capacity.

Based on the above comprehensive considerations, this work proposed the customization of VSSe material that strategically integrates the advantages of both S and Se anions through tailored design. Moreover, since the hydrothermal method usually leads to low-crystallinity materials, which exhibits many structural defects and poor stability. Therefore, PVT method was employed in this work to fabricate a high-crystallinity VSSe material, which is expected to offer optimized electronic conductivity, structural stability, and high storage capacity.

Table S2. XRD refined data of the VSS sample.

Space group	P-3m1	
Cell parameters	a (Å)	3.33454
	b (Å)	3.33454
	c (Å)	5.84319
	α (°)	90
	β (°)	90
	γ (°)	120
	Volume-Å ³	56.267
R-factors	R _{wp}	7.64
	R _p	10.6
	R _{exp}	7.67
	G _{of}	3.91

Table S3. The b values along with scan rate.

scan rate	b₁	b₂	b₃	b₄
0.2-1.0 mV s ⁻¹	1.01	0.96	0.97	1.16
2-10 mV s ⁻¹	0.84	0.86	0.87	0.91
20-100 mV s ⁻¹	0.73	0.75	0.67	0.77

References

1. S. Wang, L. Xiong, G. Yuan, T. Hu, U. Lassi, B. Wang, J. Bai, G. Wang and X. Wang, *Chem. Eng. J.*, 2023, **476**, 146883..
2. C. Liu, B. Lin, Z. Li, C. Liu, Y. Wang, W. Chen, W. Xu, M.-C. Li, S. Hong and L. Zhang, *ACS Energy Lett.*, 2025, **10**, 1795-1805.
3. H. Liu, L. Jiang, B. Cao, H. Du, H. Lu, Y. Ma, H. Wang, H. Guo, Q. Huang and B. Xu, *ACS nano*, 2022, **16**, 14539-14548.
4. S. Deng, X. Yan, Y. Jiang, A. Li, R. Zhang, Y. Qu and Z. Xie, *Chem. Eng. J.*, 2025, **503**, 158472.